

Comparison of topography and lateral spectroscopy of semiconductors

Bachelor's thesis



Fritz Haber Institute of the Max Planck Society

Department of Physical Chemistry

Electron dynamix group

Free University of Berlin

Department of Biology, Chemistry and Pharmacy

research group Structure - Dynamics - Environment - Life Sciences

submitted by: MARCO A. KAPITZKE

first assessor: Dr. JULIA A. STÄHLER

second assessor: Prof. Dr. ECKHARD RÜHL

third assessor: Dr. ROMAN FLESCHE

Contents

I	Introduction	1
II	Fundamentals	3
1	Scanning Probe Microscopy	3
1.1	Atomic Force Microscopy	3
1.2	Scanning Near-Field Optical Microscopy	4
2	Investigated systems	6
2.1	Tungsten disulfide	7
2.2	Terrylene	11
III	Experimental details	13
3	Tapping mode AFM	13
3.1	Dynamic mode AFM	13
3.2	Amplitude modulation and tapping mode	14
4	Signal processing in s-SNOM	16
4.1	Higher harmonic demodulation	16
4.2	Interferometric Detection Methods	17
5	Setup	19
6	Preparation procedure	21
6.1	Preparations for AFM	22
6.2	Preparations for s-SNOM	23
7	Tip performance	25
IV	Results and discussion	29
8	Spatial inhomogeneity in few-layered WS₂	29

9 Topography and optical nanoscopy of WS₂	33
9.1 Spatial correlation of topography and self-homodyne detection	33
9.2 Comparison of self-homodyne and pseudo-heterodyne detection	37
9.3 Spatial correlation of topography and the spectral near-field amplitude	39
10 Defects	41
10.1 Characterization of sample defects	42
10.2 Influence of substrate defects on dielectric properties	43
11 AFM imaging of ultra-thin terrylene layers	45
11.1 Surface characterization	45
11.2 Estimation of the layer thickness	47
12 Summary and outlook	48

Part I

Introduction

“What could we do with layered structures with just the right layers? [...] I can hardly doubt that when we have some control of the arrangement of things on a small scale we will get an enormously greater range of possible properties that substances can have, and of different things that we can do.”

“There’s plenty of room at the bottom”, lecture given by Prof. R. P. FEYNMAN. [1]

Fifty years after Prof. FEYNMAN’s famous lecture, A. GEIM and K. NOVOSELOV won the Nobel Prize "for groundbreaking experiments regarding the two-dimensional material graphene". [2] By reducing the dimensions of materials, novel properties based on quantum effects can emerge. As such, nanoscopic materials represent potential technical innovations for high-performance device applications that make them particularly interesting for physical and chemical research. However, many of the underlying fundamental effects have not yet been fully explored.

In the field of surface chemistry, semiconductor heterostructures, in which atomically thin layers of semiconductor materials are deposited on a substrate, are of particular interest. Here, ultra-thin layers of transition metal dichalcogenides (TMDCs) are exceptionally promising species of inorganic semiconductors, because they possess extraordinary optical and electronic properties. For example, in a novel work, an electrically driven light-emitting diode that operates at room temperature with a monolayer of a TMDC as the emissive material was demonstrated. [3] This is an important step toward microcavity light-emitting diodes as efficient planar light emitters for telecommunication applications. [4] Moreover, an effort to combine inorganic semiconductors and conjugated organic materials into novel hybrid materials – the properties of which are not achievable with any of the individual material classes alone – has been undertaken by researchers of interdisciplinary subjects. [5]

A deep understanding of nanomaterial properties is necessary to be able to effectively manipulate their characteristics. However, this requires measurement techniques that enable nanoscale imaging. Conventional microscopy, which uses visible light, has a resolution that is only about half the wavelength of the incident light. This is a result of the diffraction limit at which optical microscopy (OM) intrinsically does not have sufficient resolution. One approach to achieve topologies in the subdiffraction range is scanning probe microscopy (SPM), which resolves the sample topology. There, a sharp probe tip scans over the nanosurface and the tip-sample interaction, which is fundamentally different in nature from the light-sample interaction, is investigated. In this work, atomic force microscopy (AFM) and near-field optical microscopy (SNOM) were used. Although AFM provides topological and structural information, SNOM measurements provide a nanoscale map of chemical composition and dielectric interactions. The challenge lies in the complexity of the experimental techniques, in particular achieving an excessive, artifact-free signal in the visible range in the case of SNOM.

This work was carried out within the framework of the Collaborative Research Centre 951. [5] It is the first step in a project whose long-term goal is to develop the world’s first time-resolved scattering SNOM (s-SNOM) in the visible range to study the properties of hybrid inorganic/organic systems (HIOS) more deeply. In this thesis, the inorganic semiconductor tungsten disulfide and the organic semiconductor

terrylene were investigated by means of AFM and s-SNOM. It had two main objectives: one, the commissioning of a commercial s-SNOM and its characterization with respect to different measurement methods, namely, self-homodyne and pseudo-heterodyne detection; the other, the comparison of high-resolution topography and lateral microscopy images of the investigated systems. This comparison provides new insights about the chemical, structural and electronic properties of the samples, which cannot be achieved by conventional techniques.

First investigations on the influence of the topography on optical effects by examining a transition metal chalcogenide using AFM reveal a special dependence of the optical response. Crucial factors involved in achieving proper performance for the s-SNOM are identified. Using tungsten disulfide, it was demonstrated that the self-homodyne technique contains spatially dependent background radiation. A comparison of self-homodyne and pseudo-heterodyne detection reveals that pseudo-heterodyne detection is a successful experimental practice eliminating the impact of spatially dependent scatter phenomena. Spatial irregularities have been resolved on the nanoscopic length scale using AFM and s-SNOM in a pseudo-heterodyne manner. A relationship between topography and the artifact-free lateral optical signal – a lower sample topography is accompanied by a higher optical signal – was identified, but with deviations. Some depressions of the topography show clear optical signals. The comparison of both SPM methods reveals that the apparent height found in the topography does not reflect the actual sample thickness, but substrate defects are also measured. The conclusion has been drawn that AFM or s-SNOM alone are not sufficient to distinguish between actual or apparent defect-induced sample properties; only the combination of both topologies provides the needed information. The influence of defects in tungsten disulfide on AFM and s-SNOM recordings was investigated. In addition, a surface characterization was performed using the organic semiconductor terrylene. It was shown that, in this case, the apparent height of the topography is equal to the sample height.

The thesis is divided into four parts and 12 chapters. After this introduction, the second part outlines the theoretical background of this work, concerning the microscopy used and the investigated systems. The third part focuses on experimental details. This includes the microscopic techniques used, the optical measurement setup, and the laser system used for s-SNOM, as well as the preparation of the measurements and tip performance. First results on the influence of the topography on optical effects are discussed at the beginning of the fifth part. Next, the central questions of the present work, namely, the comparison of self-homodyne and pseudo-heterodyne detection as well as the relationship between topography and the lateral optical signal, are discussed using a TMDC. After the sample and substrate defects are characterized, this work is completed with an investigation of the surface structure of an organic thin film.

In conclusion, this thesis provides an initial step towards the study of a HIOS using s-SNOM in the visible light regime. The next achievable step in this project is the combination of the semiconductors tungsten disulfide and terrylene. In the medium-term, spatially and time-resolved studies using pulsed laser sources will be carried out.

Part II

Fundamentals

This part opens with a description of the experimental microscopy techniques used in this work. Then the structural, electronic and optical properties of the investigated systems are described.

1 Scanning Probe Microscopy

Scanning probe microscopy (SPM) summarizes all types of microscopy in which the image is not obtained with an optical projection, but via the interaction of a sharp probe with the sample. Depending on the type of interaction, a distinction is made between different SPM types. This chapter presents the basics of atomic force microscopy and scanning near-field optical microscopy.

1.1 Atomic Force Microscopy

The atomic force microscope (AFM) is an important imaging technique in the field of surface chemistry which is used to investigate the morphology of samples down to the nanometer scale. The technology was introduced in 1986 by G. BINNIG et. al. [6] and was further developed by Q. ZHONG et. al. [7] and others.

Basic principle

The basic components are the cantilever, to which a tip is attached, the optical recognition system and the feedback electronics, see figure 1. It uses the sharp tip to measure interatomic interactions between the tip and the sample.

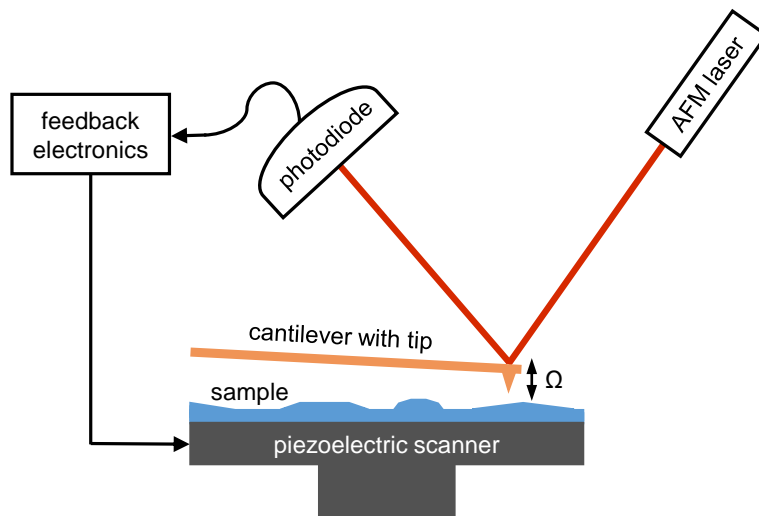


Figure 1: Schematic setup of an AFM.

The tip is moved across the surface in raster fashion, measuring the tip-sample forces at each pixel. From the magnitude of this force, the surface morphology is obtained. It is derived from the behavior of the cantilever because, during the scanning process, the cantilever behaves like a spring that bends under the influence of those forces. This bending is measured by using a laser beam reflection from the surface of the cantilever onto a photodiode detector. The displacement of the laser spot produces feedback that initiates a piezo crystal mounted at the base of the sample to contract or expand. The height h of the sample can be inferred from the corresponding change of its z -distance. The surface height information is acquired by tracking the deflection of the sample induced by the piezo crystal. [8]

Tip-sample forces

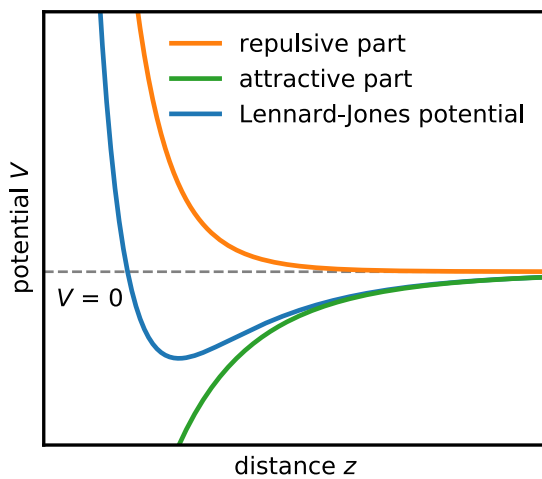


Figure 2: 6,12-LENNARD-JONES Potential.

Because the basic idea of AFM is to measure the acting forces between the tip and the surface, it is necessary to discuss those first. The total force between tip and sample is composed of several attractive and repulsive contributions. For large distances between two particles, the attracting VAN-DER-WAALS forces predominate. They arise through the spontaneous formation of fluctuating electric dipoles [9], polarization [10] and electrostatic interactions between charges. [11] The repulsive forces that emerge at a small distance are mainly caused by the overlap of inner closed shells. According to the PAULI exclusion principle, two electrons cannot occupy the same state. [12] That is why electrons have to deviate to higher-lying electronic states. In approximation, both attractive and repulsive interactions between un-

charged and non-bounded atoms can be described by the 6,12-LENNARD-JONES potential [13] as

$$V_{LJ}(z) = 4V_0 \left[\left(\frac{\sigma}{z} \right)^{12} - \left(\frac{\sigma}{z} \right)^6 \right], \quad (1)$$

where V_0 is the depth of the potential well and z describes the distance between the tip and the sample. The parameter σ is given by $V_{LJ}(\sigma) = 0$. A graph of the 6,12-LENNARD-JONES potential and its components is shown in figure 2.

1.2 Scanning Near-Field Optical Microscopy

Although surface scanning techniques, such as AFM, have been introduced as highly successful methods for the spatial investigation of surfaces, they do not provide information about optical properties. Scanning nearfield optical microscopy (SNOM) enables optical imaging by exploiting the properties of near-fields. In addition to the optical data, the topography of the measured surface is received as well, because an AFM is integrated into the setup.

Basic principle

The idea to exceed the diffraction limit for microscopy by probing a near-field originated in 1928 from E. SYNGE [14], but it was first implemented in 1984 using an aperture-SNOM (a-SNOM). [15] Today, a distinction is made between the a-SNOM, in which a coated glass fiber or silicon tip with small aperture is used as a light source or collector, and the later developed scattering-SNOM (s-SNOM), in which a metal tip is used as a light source. [16] In the following, the s-SNOM will be discussed in more detail, since this method was used during this work. As mentioned, it is based on an AFM system, but there is a significant extension. The apex of the tip is illuminated by a focused laser beam using a parabolic mirror. The backscattered light following the illumination is detected, as shown in figure 3.

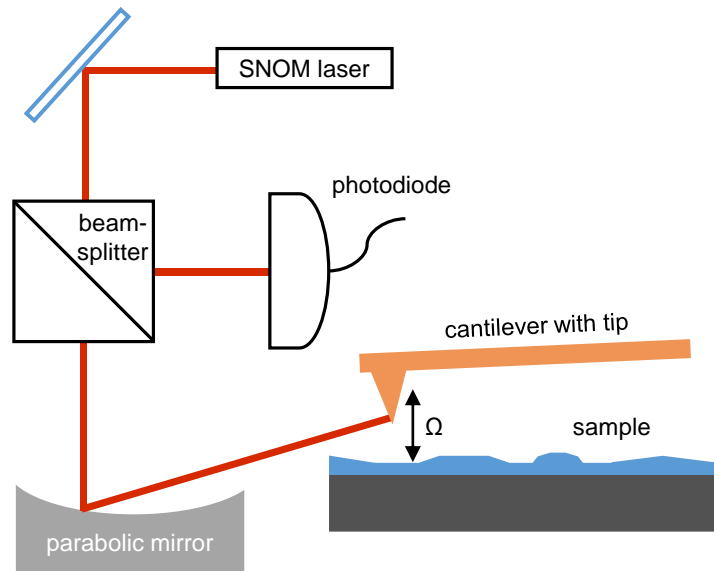


Figure 3: Schematic setup of a s-SNOM.

The illuminated tip polarizes the sample because of the lightning rod effect [17], which then acts on the tip and creates a near-field interaction [18] that is specific for the sample and the tip material. It can be expressed very generally by the following equation [19]:

$$E_{\text{sca}} = \sigma_{\text{sca}} E_{\text{in}} . \quad (2)$$

Here, E_{in} is the electric field component of the incident and E_{sca} of the scattered laser light. On this occasion, it must be taken into account that the acquired signal is the entire backscattered laser light following the illumination path. [20] In other words, not only near-field enhanced, but scattered light from other origins, that is referred to as background, is detected as well. Therefore, the quantity E_{sca} can be divided into its components:

$$E_{\text{sca}} = E_{\text{nf}} + E_{\text{bg}} . \quad (3)$$

Here, E_{nf} denotes to the near-field scattering and E_{bg} to the background scattering signal. The latter is

much larger in absolute values than the near-field signal. The background is generated by reflections or scattering from the tip shaft, cantilever, or sample surface. [21] This is problematic because the background signal contains no information about the sample and covers the near-field signal. Fortunately, there are different techniques to suppress the harmful background portion of the signal, which can be partly combined. The disentanglement of E_{nf} and E_{bg} is an important part of this thesis work and will be dealt with in chapter 4. The next paragraph focuses on how the near-field actually emerges.

Near-field enhancement

The tip-sample interaction that creates the near-field can be described analytically by approximation models. The goal of those is to find an expression for the effective polarizability α_{eff} , because it is proportional to the enhancement of the optical near-field E_{nf} . Two common models that achieve this are the dipole model and the finite dipole model. Although the latter also allows quantitative predictions [22], the more frugal dipole model is sufficient for the purposes of this work and nevertheless allows qualitative statements.

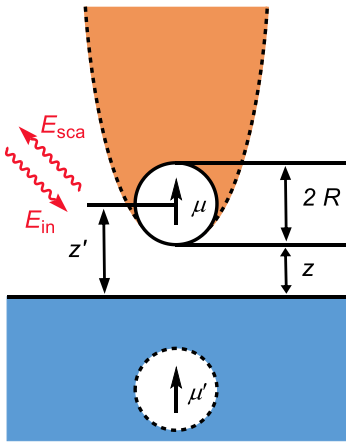


Figure 4: Illustration of the dipole model.

In the dipole model, the tip is simplified to a point dipole μ , see figure 4. The AFM tip is approximated through a small circle with radius r ; z represents the distance between tip and sample. It is assumed that the dipole is polarized vertically due to the elongated shape of the tip. [23] For the effective polarizability α_{eff} , one finds [24]

$$\alpha_{\text{eff}} = \alpha \left\{ 1 - \frac{\alpha \beta (\epsilon_{\text{sample}})}{16\pi (r + z)^3} \right\}^{-1}, \quad (4)$$

where α is the polarisability of the sphere and $\beta (\epsilon_s)$ the polarisability of the sample. The latter is determined by the complex-valued permittivity ϵ_{sample} of the sample through:

$$\beta (\epsilon_{\text{sample}}) = \frac{\epsilon_{\text{sample}} + 1}{\epsilon_{\text{sample}} - 1}. \quad (5)$$

The permittivity ϵ_{sample} is only a scalar for special cases; it usually depends on several parameters, such as the frequency and direction of the applied field or the temperature – which is why the name dielectric function better reflects the properties of this quantity. The dielectric function according to the irradiated laser frequency $\epsilon_{\text{sample}}(f)$ is of great interest for the enhancement of the near-field interaction, as it will become apparent later.

2 Investigated systems

During the course of this work, two systems – an inorganic and an organic one – were studied: tungsten disulfide (WS_2) absorbed onto silicon dioxide (SiO_2) and terrylene absorbed onto sapphire. Few-layer systems of both substances were studied.

2.1 Tungsten disulfide

Atomically thin crystals have attracted much attention since the discovery of graphene. A number of fascinating phenomena occur in those so-called VAN-DER-WAALS systems due to a drastic reduction of the dimension. Among the particularly exciting systems of this kind are the transition metal dichalcogenide (TMDC) monolayers. [25] Many interesting phenomena often occur in samples with a thickness of a few monolayers.

Structure

WS_2 is one of about 60 TMDCs. The structure of the bulk crystal consists of layered hexagonal structures that are held together by interlayer VAN-DER-WAALS forces. [26] Figure 5a shows the hexagonal close-packed crystal structure of WS_2 . Upon the transition from three-dimensional to quasi-two-dimensional materials, the inversion symmetry disappears, which is only present in materials with an even number of layers. TMDCs primarily contain three different allotropes, which lead to different electronic phases [27]:

- 2H phase: The chalcogen atoms are trigonally prismaticly arranged and the monolayers belong to the point group $P\bar{6}m2$, cf. figure 5b.
- 1T phase: The chalcogen atoms are arranged trigonally-antiprismaticly and the monolayers belong to the point group $P\bar{3}m1$.
- 1T' phase: The 1T' phase is derived from the 1T phase by distortion. Accordingly, the 1T' material is triclinic, i.e. it belongs to the space group $P\bar{1}$.

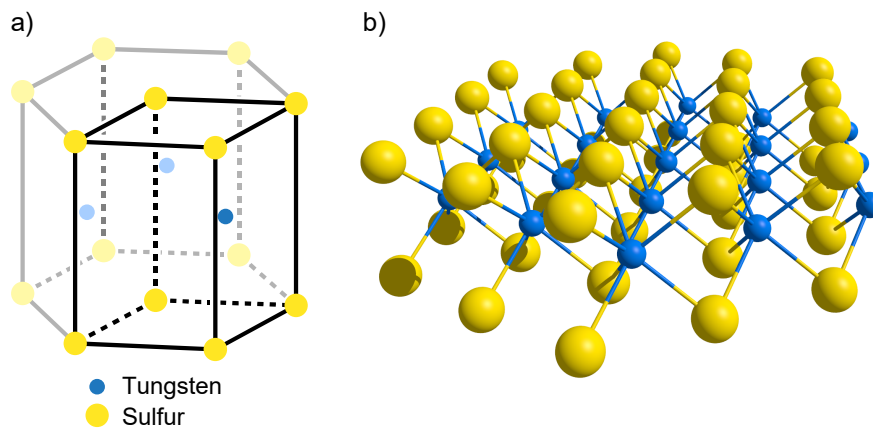


Figure 5: (a) Hexagonal close-packed crystal structure with a highlighted unit cell; (b) Hexagonal 2H WS_2 monolayer seen from the side.

The 2H phase is energetically most favorable and shows semiconducting behavior. The metastable 1T phase and the 1T' phase are conductors. [28, 29] In the following, only the primarily interesting 2H phase is considered. These samples are usually prepared by exfoliation or chemical vapor deposition (CVD).

VAN-DER-WAALS systems can be mechanically separated to isolate atomically thin flakes, as graphene can be produced from graphite. In CVD, a chemical reaction on the heated substrate surface causes the gaseous sample to be separated as a solid component. [30]

Description of electrical properties in reciprocal space

By reducing the number of layers of WS_2 crystals, the VAN-DER-WAALS interactions between adjacent atomic layers are reduced as well. For a monolayer, the result is, in comparison to the bulk crystal, an electronic band structure in reciprocal space as shown in figure 6a: The bulk crystal (orange) is an indirect [31] and the monolayer (blue) a direct [32] semiconductor. The bandgap magnitudes E_{gap} for direct and indirect semiconductors differ in the literature. This is because the absolute position of the bands and the quantum-mechanically forbidden zone are experimentally difficult to determine. Moreover, the exact bandgap value is also strongly dependent on external influences on thin layers, which will be explained in more detail in the next section. To give an idea of the order of magnitude for the gaps: in bulk crystals the indirect bandgap magnitude $E_{\text{gap}}^{\text{ind}}$ amounts to approximately 1 eV and for monolayers the direct bandgap magnitude $E_{\text{gap}}^{\text{dir}}$ is about 2 eV. If the electronic band structure is not considered along a path of high symmetry in the BRILLOUIN zone, but along the base vectors k_x and k_y (in reciprocal space), the the so-called "valleys" around the K symmetry points manifest. Figure 6b shows the highest occupied electronic state of the valence band (VB) and the lowest unoccupied state of the conducting band (CB). Here, the valleys and the direct band gaps $E_{\text{gap}}^{\text{dir}}$ are visible. It is also common to refer to the extrema along one-dimensional paths as valleys. [33]

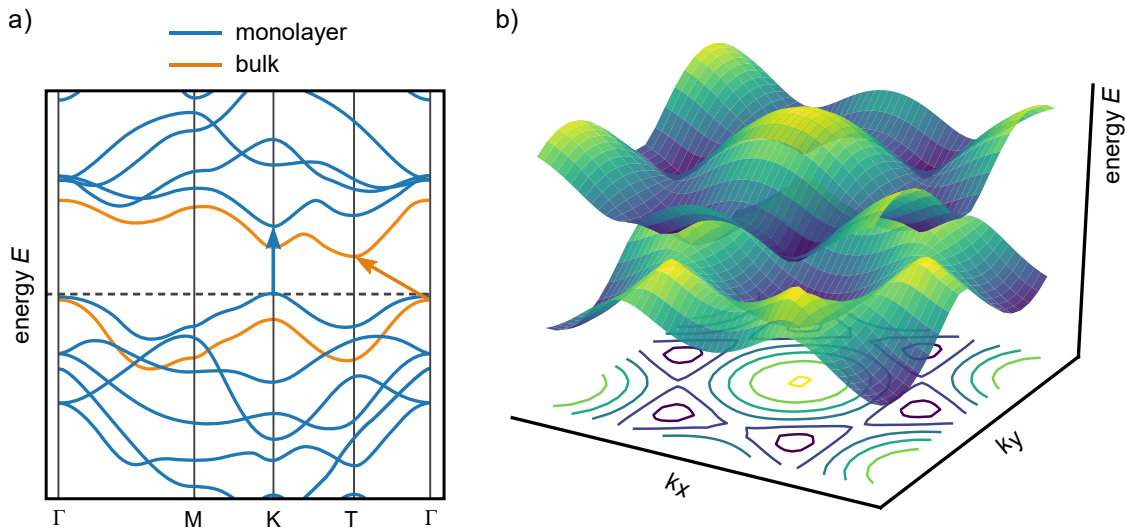


Figure 6: Schematic band structure of 2H WS_2 along (a) a one-dimensional path of high symmetry, after ref. [32], and (b) the base vectors k_x and k_y .

The spin-orbit interaction in TMDCs is much stronger than in graphene, one of the best-known quasi-two-dimensional materials. The origin of this distinction lies in the involvement of the transition metal d-orbitals of tungsten. This spin-orbit coupling has consequences: the degenerate valleys at the K points

2 Investigated systems

split up in two configurations if an external field is applied. [34] The result is the generation of alternating, but energetically equivalent, K and K' symmetry points in the corners of the BRILLOUIN zone for which different optical selection rules apply. [33]

However, for this thesis, only the energetic splitting Δ of states is of particular interest: In the CB, the splitting of the highest occupied state Δ_{CB} is slightly higher than 0.4 eV [35, 36] and significantly higher than that of the lowest unoccupied state Δ_{VB} in the VB, which is only a few meV. [36] Therefore, the splitting of the VB is neglected in the following, so that a degenerate first excited state can be assumed in approximation, as shown in figure 7. The splitting of the CB enables the excitation of two excitons in the visible range, which are called A and B.

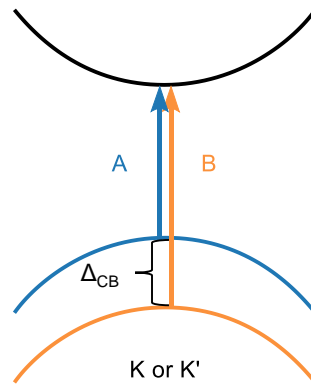


Figure 7: Schematic representation of the splitted bands, with the approximation that $\Delta_{VB} = 0$ eV.

Dielectric and optical properties

The two excitons A and B are observable in the imaginary part of the dielectric function $\text{Im}(\epsilon(f))$, which corresponds to both refraction and absorption of the material at a given frequency f or energy E . [37] In case of dielectric function shown in figure 8, the 2H WS₂ sample was deposited onto a SiO₂ substrate. This heterostructure system was studied in the thesis.

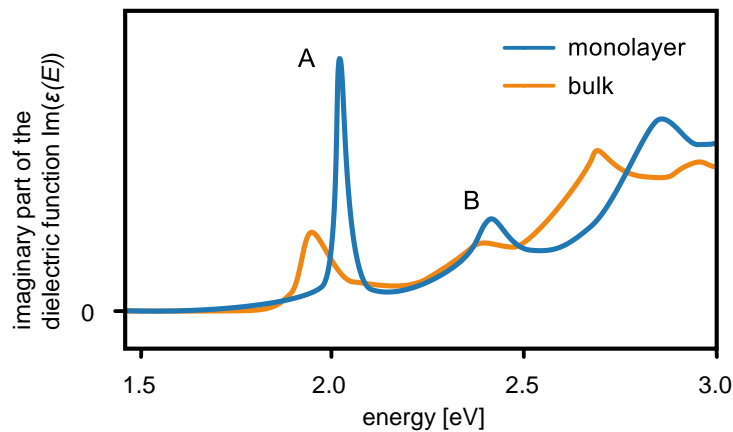


Figure 8: Imaginary part of the dielectric function $\text{Im}(\epsilon(E))$ of 2H WS₂ on SiO₂, after ref. [37].

One of the most interesting properties of ultra-thin materials is the reduced shielding against the change in the dielectric environment, cf. figure 9. Depending on which substrate the sample is in contact with, the measured dielectric function for atomically thin layers can change significantly, i.e. in approximation the following relationship applies:

$$\varepsilon_{\text{measured}}(f) = \varepsilon_{\text{sample}}(f) \circ \varepsilon_{\text{substrate}}(f). \quad (6)$$

Here, the symbol \circ represents a not more closely defined binary operation that describes the linkage of $\varepsilon_{\text{sample}}(f)$ and $\varepsilon_{\text{substrate}}(f)$.

Considering the band structure and the dielectric function, properties of monolayer and bulk were compared, mainly. But to what extent do the properties of monolayers transfer to few-layer systems? For this purpose, it is necessary to discuss how the basic excitonic – and thus optical – properties of atomically thin layers differ from those of the same but extended material. The origin of this behavior of bulk and thin materials in real space is schematically illustrated in figure 9a and b.

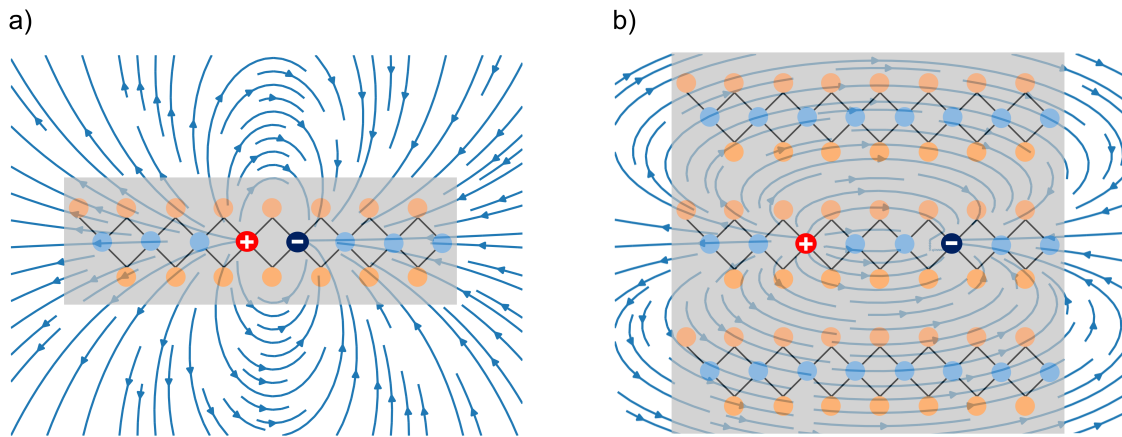


Figure 9: Schematic representation of an exciton as well as $\varepsilon_{\text{sample}}(f)$ for (a) monolayers and (b) multilayers.

Because of the quasi two-dimensionality, the exciton from figure 9a is restricted to the plane. Thus, the electron-hole interaction increases and the system reaches an energetically deeper state, resulting in a shorter binding distance. [38] The thinner the material, the larger the bandgap E_{gap} will turn out. The absorption of few-layer systems is therefore slightly red-shifted compared to that of monolayers. The intensity of the (overall) absorption naturally increases for a larger number of layers. Interestingly, when studying photoluminescence (PL) spectra of different thicknesses, the PL quantum yield for thinner TMDCs is significantly higher than for thicker ones. The characteristics associated with the indirect transition can be observed, too. For bulk crystals, the PL finally decreases significantly and shows only emissions associated with the indirect transition. [39]

2.2 Terrylene

Terrylene ($C_{30}H_{16}$) is a conjugated organic semiconductor with a high fluorescence quantum yield that also has an exquisite sensitivity for optical transitions, e.g. to electric fields. [40, 41] Therefore, it has a potential application range in thin film electronics. Its skeletal formula is shown in figure 11.

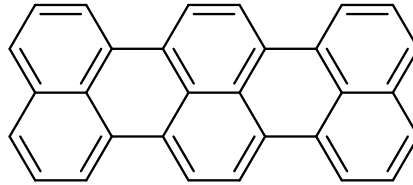


Figure 10: Skeletal formula of terrylene.

By absorbing a photon that matches the energy difference between the initial and final state, terrylene can undergo an electronic transition. As most organic semiconductors, it is characterized by localized and strongly bound excitons. As shown in figure 12a, the ground-state of terrylene is the singlet S_0 state. The probability of a spin-allowed vertical transition, assuming the BORN-OPPENHEIMER approximation, is proportional to the square of the transition matrix element. [42]

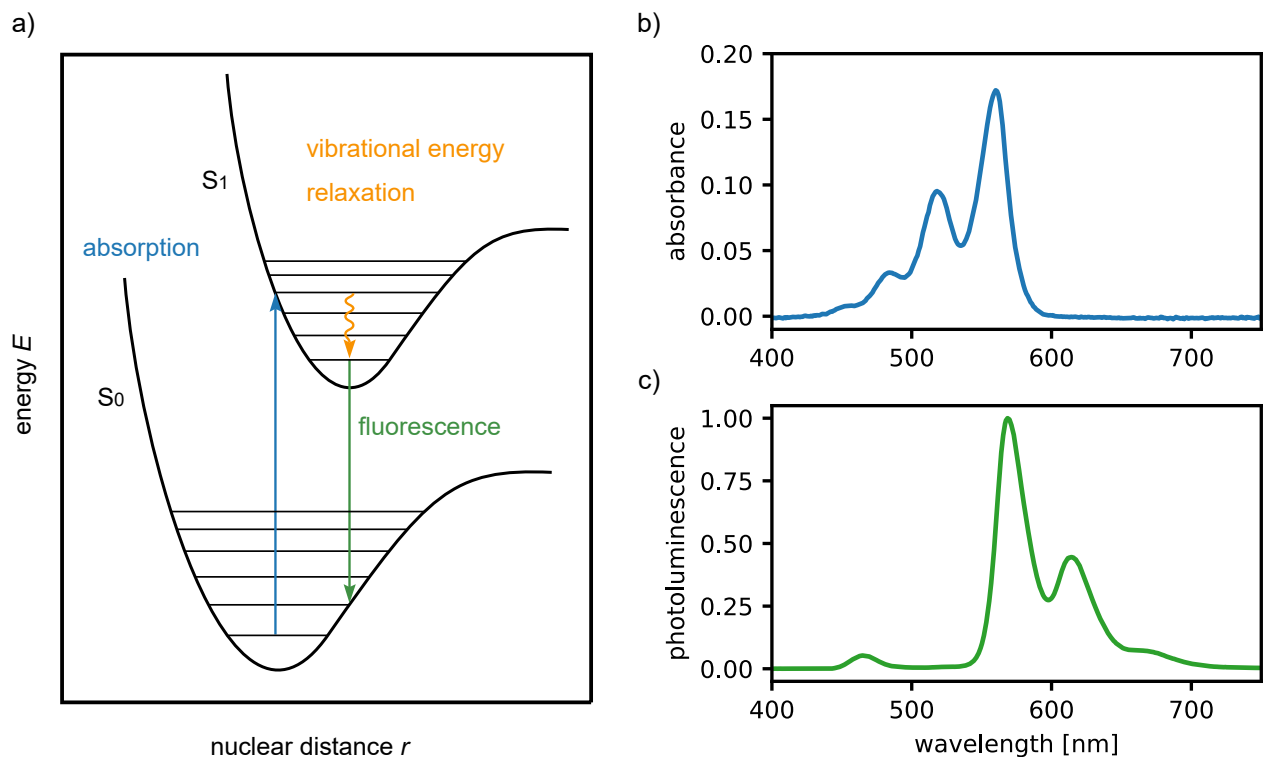


Figure 11: (a) Illustration of the electron dynamix within vibronic levels in terrylene; (b,c) Absorption and PL spectrum of terrylene in solution. The measurement data were received from B. T. BONKANO.

After a photoexcitation into the first excited singlet state S_1 , the excess energy can be released by different relaxation processes, both radiative and non-radiative. The radiative relaxation is generally called photoluminescence (PL) and, when it occurs within electronic states of the same spin multiplicity, fluorescence. In addition, relaxation (phosphorescence) or transitions (inter-system crossing) can occur within electronic levels of the different spin multiplicity and are quantum-mechanically forbidden. This prohibition can be lifted by spin-orbit coupling. The lowest excited triplet state T_1 of terylene lies below the S_1 state, but it is populated with a very low probability. While a molecule is in its triplet state, it can neither absorb nor emit photons and is, therefore, “dark”. [43]

The absorption spectrum of terylene in figure 12b shows absorption bands corresponding to the vertical vibronic transitions from S_0 to S_1 . The comparison of the absorption spectrum and the photoluminescence spectrum, cf. figure 12c, reveals a red-shift, the so-called STOKES shift, of the absorption bands. It is due to non-radiative vibrational energy relaxation, as shown in the orange relaxation path in figure 11a.

Because of KASHA’s rule, PL spectroscopy only addresses the lowest excited state directly. But the “dark” T_1 state can act as a potential trap for an excitonic population in (appropriate) hybrid systems. [44]

Part III

Experimental details

This chapter is devoted to the description of the experimental tools used in this work. Valuable experimental data cannot be extracted until refined methods are used. Chapters 3 and 4 discuss the methods used for data acquisition. Their comprehension is essential for the interpretation of the measurement data. Chapter 5 presents the optical setup of this thesis. Furthermore, an experiment requires a well defined, reproducible measurement routine, which is discussed in chapter 6. Finally, the influence of the tip on the AFM and s-SNOM performance is reviewed.

3 Tapping mode AFM

Because the AFM is an extremely flexible instrument, it is capable of operating in three general modes: the contact mode, the non-contact mode, and the tapping mode. [45] While the repulsive forces are dominant in contact mode, attractive forces prevail in the non-contact mode. In the tapping mode, which was used during this thesis, both attractive as well as repulsive forces can be observed. [46] Because the tapping mode is a dynamic mode, the movement of the cantilever using the harmonic approximation is discussed first.

3.1 Dynamic mode AFM

In dynamic mode, a weakly perturbed cantilever can be mathematically described by a driven harmonic oscillator with damping. [47] The cantilever force $F_{ts}(z)$ is derived from the force gradient $\partial/\partial z V_{LJ}(z)$ and is approximated by that of a HOOKEAN linear spring with the spring constant k . The driving force $F_{drive}(z)$ is due to the sinusoidally external movement of the cantilever base and is approximated by a HOOKEAN linear spring as well. Moreover, the corresponding oscillation can be written as $z_{drive}(t) = A_{drive} \cos(\Omega t)$, where A_{drive} denotes the excitation amplitude. Additionally, damping has to be considered, which is modeled by a friction force $F_{damp}(z) = -m\xi \partial/\partial t z$, where ξ is the dimensionless coefficient of friction. The equation of motion for the sum of the operating forces becomes

$$\sum_j F_j(z) = F_{ts}(z) + F_{drive}(z) + F_{damp}(z) = -k[z - z_{drive}(t)] - m\xi \frac{\partial}{\partial t} z = m \frac{\partial^2}{\partial t^2} z, \quad (7)$$

where m is the mass of the cantilever. One can solve this inhomogeneous differential equation of second order by finding a complex solution. However, only the real part is considered. The solution $z_{cant}(t)$ describes the motion of the cantilever and introduces a (mechanical) phase difference ϕ between the excitation amplitude A_{drive} and oscillation amplitude A_{cant} of the cantilever:

$$z_{cant}(t) = A_{cant} \cos(\omega t + \phi). \quad (8)$$

Here, ω is the angular frequency of the cantilever. From here one can find the amplitude dependency

$$A_{\text{cant}} = \frac{A_{\text{drive}} Q}{\sqrt{\left(\frac{\omega}{\Omega_0}\right)^2 + Q^2 \left[1 - \left(\frac{\omega}{\Omega_0}\right)^2\right]^2}} \quad (9)$$

and the phase dependency on the frequency

$$\varphi = \arctan \left(\frac{\frac{\omega}{\Omega_0}}{Q \left[1 - \left(\frac{\omega}{\Omega_0}\right)^2\right]} \right), \quad (10)$$

where Ω_0 is the (angular) resonance frequency. The quality factor Q is a dimensionless parameter that quantifies how underdamped an oscillator is. It influences the sharpness of the resonance and the phase, cf. figure 12a, and is given by

$$Q = \frac{\Omega_0}{\xi}. \quad (11)$$

Cantilevers with a high quality factor Q enable an increased image resolution and improved sensitivity. [48]

3.2 Amplitude modulation and tapping mode

The amplitude, the resonance frequency and the phase shift represent parameters that hold a connection of the movement of the cantilever with the surface topography. Therefore, all of them can be used as a feedback parameter to track the morphology of the surface. [49]

For the experimental setup of this work, the amplitude modulation feedback was used in which the excitation amplitude A_{drive} and the resonance frequency Ω_0 were kept constant. Usually, the cantilever is driven at $\omega = \Omega$, close to its resonance frequency. On the other hand, Ω_0 is (for weak disturbances) non-linearly dependent on the effective force gradient $\partial/\partial z F(z) = \partial^2/\partial z^2 V_{\text{LJ}}(z)$, thus a function of the tip-sample distance z . Figure 12a illustrates that cantilever amplitude A_{cant} is a function of the difference $\Omega - \Omega_0$, so the functional relationship $A_{\text{cant}}(\Omega_0(\partial/\partial z F(z)))$ applies. The change of the tip-sample distance z results in a shifted resonance frequency $\tilde{\Omega}_0$ and, therefore, also in a change of the actual amplitude \tilde{A}_{cant} . As shown in figure 12b, with a resonance frequency shift $\Delta\Omega_0$, the phase difference between the driving oscillation and the detected cantilever oscillation is changed by $\Delta\phi$ as well.

3 Tapping mode AFM

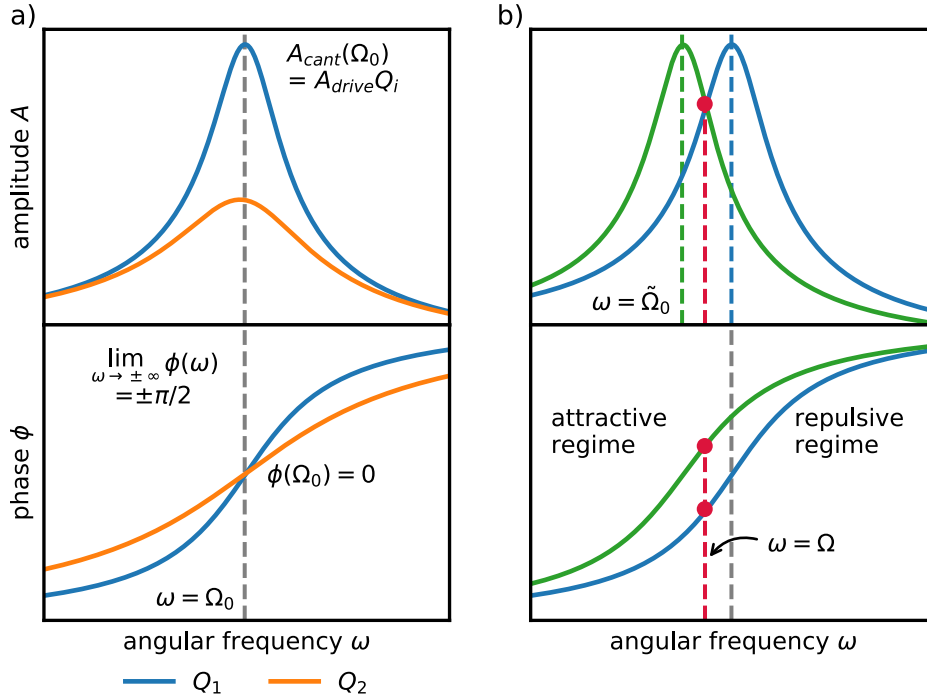


Figure 12: (a) Influence of quality factor Q (with $Q_1 > Q_2$) on the cantilever amplitude A_{cant} and phase difference ϕ ; (b) Schematic representation of the amplitude modulation operation mode.

While operating in tapping mode, the cantilever is excited into oscillations with a large amplitude of up to 100 nm. In principle, amplitude modulated AFM can also be performed in non-contact mode, but this mode is not suitable for experiments in the air because the cantilever is influenced by adsorbed water layers. [45] Also, in comparison to contact mode AFM, tapping mode is more gentle to the tip as well as surface and, therefore, the preferred method. Admittedly, the assumption of a weakly perturbed cantilever no longer applies to the large amplitudes used in tapping mode. Here, because of anharmonicity, the resonance curve is distorted and the frequency shift predicted by the harmonic approximation is not correct. [47] Still, the functional principle remains the same and harmonic models are useful to provide some intuition for the phase shift that occurs in tapping mode, too. That is why, in the following, the harmonic approximation is assumed to relate phase shifts and excitation frequency. By measuring the shift of the phase $\Delta\phi$, a phase-contrast image is acquired. Those images provide an immediate determination whether the acting net forces per tapping cycle were attractive or repulsive, which defines an operating regime. [46] Since the feedback-loop restores the original amplitude A_{cant} , phase changes are always considered as relative to the initial resonance frequency Ω_0 . The presence of an abrupt change of the tip-sample distance z_0 can lead to an alteration of the acting net forces, which, however, cannot be detected in the topography image. [46] Since the function $\phi(\omega)$ is – in the harmonic approximation – bijective, the phase image will show a switch of the operation regime, cf. figure 12b. Moreover, the phase-contrast is able to reveal certain surface properties, especially for rough ones, which are obscure in topographic images. [50] It arises from an enhanced tip-sample interaction. [51]

4 Signal processing in s-SNOM

As mentioned in Section 2.1, the signal contains an undesirable background component. To remove this malicious background signal, sophisticated background suppression methods such as harmonic demodulation and interferometric signal detection schemes, were developed. The following were implemented during the thesis.

4.1 Higher harmonic demodulation

An omnipresent background suppression method is the higher harmonic demodulation. It utilizes the strong, nonlinear sample dependence on the tip-sample distance $z(t)$ that the near-field signal shows, compare equation (4). The tip is periodically excited as in AFM. Since tapping mode is used, the tip-sample distance can be described by $z(t) = z_0 + A_{\text{cant}} \cos(\Omega t)$. Because of the large oscillation amplitude A_{cant} , a distinction between the near-field signal and the background signal can be made. The reason for this is that the far-field interaction $E_{\text{bg}}(z(t))$ shows a much weaker z dependence compared to $E_{\text{nf}}(z(t))$, under the condition that the tip is in the immediate vicinity of the sample, i.e. $z \ll \lambda$. [52] Consequently, the electric field and so the signal intensity $I_d(z(t)) = |E_{\text{sca}}(z(t))|^2$ is described as a sinusoidal shape. That is why the FOURIER transform of $I_d(t)$ into the frequency domain provides a signal with higher harmonics $n\Omega$, $n \in \mathbb{N}$, which is schematically shown in figure 13. The higher harmonics are due to the stronger z -dependency, prominently generated by $E_{\text{nf}}(z(t))$, hence their frequency contributions also increasingly contain near-field components in absolute values. That is why they are preferably evaluated.

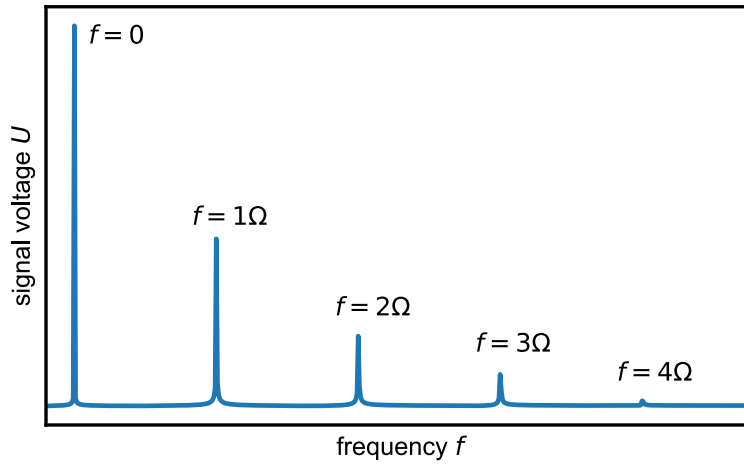


Figure 13: Simulated FOURIER transform of the (self-homodyne) signal intensity $I_d(t)$, revealing the harmonics $n\Omega$ in the frequency-domain. Here, the intensity $I_d(f)$ was converted into a signal voltage $U(f)$ by the detector.

However, it must be noted that the absolute signal strength decreases when studying higher harmonics, meaning that noise effects will play a more important role – at worst, they can completely mask the signal. Therefore, an optimal harmonic n , containing a sufficient signal strength and an adequate near-field proportion of the detected signal, must be chosen. [19]

4.2 Interferometric Detection Methods

Nevertheless, higher harmonics demodulation is not sufficient for avoiding artifacts, [53] because harmonic demodulation can not entirely suppress the background scatter contribution, regardless of the demodulation harmonic. [54] To solve this, E_{nf} can, in addition, be enhanced through interferometric detection methods, namely self-homodyne and pseudo-heterodyne detection. [55]

Self-homodyne detection

In self-homodyne detection, a near-field amplification is achieved by interfering E_{nf} with the strong background signal E_{bg} . Since $I_d = |E_{\text{sca}}|^2$ applies, with equation (3) it follows:

$$I_d = |E_{\text{nf}} + E_{\text{bg}}|^2 = (E_{\text{nf}} + E_{\text{bg}}) (E_{\text{nf}} + E_{\text{bg}})^* . \quad (12)$$

The term $(E_{\text{nf}} + E_{\text{bg}})^*$ denotes the complex conjugate of $(E_{\text{nf}} + E_{\text{bg}})$. Expression (12) results in:

$$I_d = |E_{\text{nf}}|^2 + |E_{\text{bg}}|^2 + 2 |E_{\text{nf}}| |E_{\text{bg}}| \cos (\Delta\varphi t) . \quad (13)$$

Here, $\Delta\varphi$ is the optical path difference between the background phase φ_{nf} and the near-field phase φ_{bg} . The terms $|E_{\text{nf}}|^2$ and $|E_{\text{bg}}|^2$ are negligibly small for higher harmonics. This can be shown by expressing the components E_{nf} and E_{bg} as a FOURIER series [56] and thus:

$$2 |E_{\text{nf}}| |E_{\text{bg}}| \cos (\Delta\varphi t) . \quad (14)$$

The advantage of this detection method is that it is comparatively easy to perform. However, it has a big disadvantage. It is not possible to determine the actual amplitude, which in the following (mathematically somewhat unclear) is referred to as the near-field amplitude, of the signal. The reason is that no stable phase information $\Delta\varphi$ is obtained because φ_{bg} results from random scattering events and is practically unknown. Therefore, only a quantity, which is called near-field magnitude in the following, multiplied by an undefined phase factor $\cos (\Delta\varphi t)$ can be determined using self-homodyne detection.

Pseudo-heterodyne detection

In pseudo-heterodyne detection, the setup is extended by a reference arm, see figure 14. The reference arm consists of an oscillating mirror – basically a MICHELSON interferometer – which is modulated with the frequency M . The amplification of the near-field signal now comes through the reference beam E_{ref} .

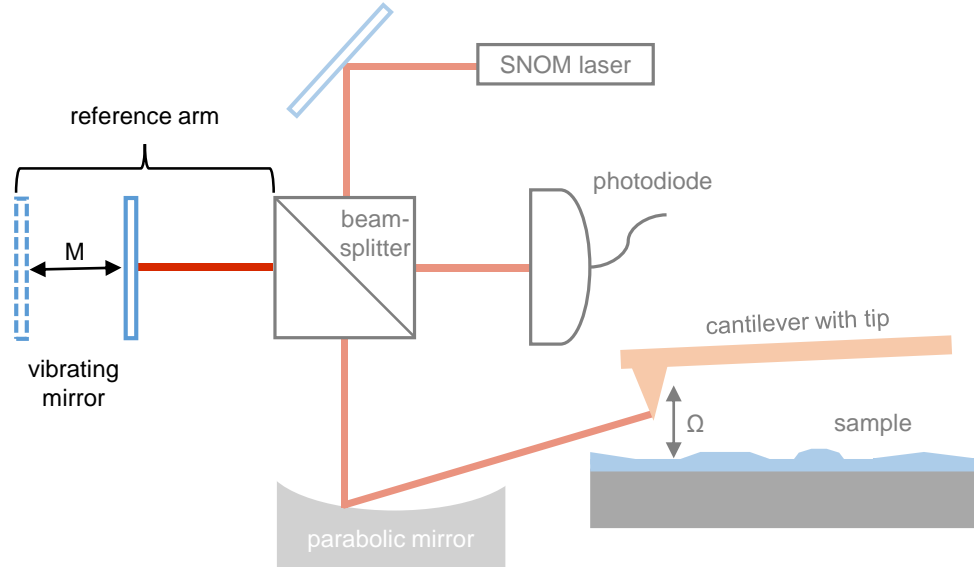


Figure 14: Schematic detection scheme for pseudo-heterodyne detection. No more than a reference arm has been added to the setup.

The interference of E_{nf} and E_{bg} with E_{ref} generates sidebands in the frequency domain at frequencies $f = n\Omega + mM$, where $n, m \in \mathbb{N}$. The corresponding electrical signal $U(f)$ is shown in figure 15, where the harmonics $n\Omega$ are blue and the sidebands mM are orange. It should be noted that the harmonics in pseudo-heterodyne detection have different absolute values than in self-homodyne detection.

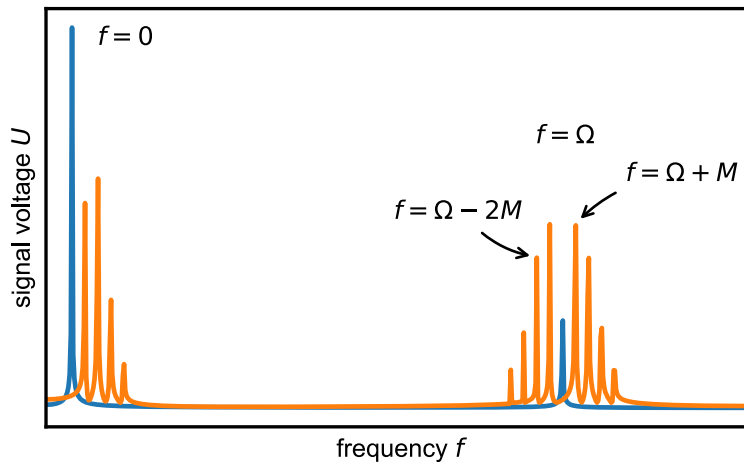


Figure 15: Simulated FOURIER transform of the pseudo-heterodyne signal intensity $I_d(t)$, revealing the harmonics $n\Omega$ and the sidebands mM in the frequency-domain.

This becomes obvious when looking at the detected signal. With the modification by the reference beam, one obtains:

5 Setup

$$I_D = |\mathbb{E}_{\text{nf}} + \mathbb{E}_{\text{bg}} + \mathbb{E}_{\text{ref}}|^2 = (\mathbb{E}_{\text{nf}} + \mathbb{E}_{\text{bg}} + \mathbb{E}_{\text{ref}}) (\mathbb{E}_{\text{nf}} + \mathbb{E}_{\text{bg}} + \mathbb{E}_{\text{ref}})^* . \quad (15)$$

After expanding (15) and exploiting the properties of complex numbers one finds:

$$I_D = |\mathbb{E}_{\text{nf}}|^2 + |\mathbb{E}_{\text{bg}}|^2 + |\mathbb{E}_{\text{ref}}|^2 + 2\text{Re} (\mathbb{E}_{\text{nf}}\mathbb{E}_{\text{bg}} + \mathbb{E}_{\text{nf}}\mathbb{E}_{\text{ref}} + \mathbb{E}_{\text{bg}}\mathbb{E}_{\text{ref}}) . \quad (16)$$

Here, the FOURIER series representation of \mathbb{E}_{ref} is given by [57]

$$\mathbb{E}_{\text{ref}} = \sum_m \sigma_{\text{ref},m} \exp (i \{ \gamma \sin (Mt) + \Delta\chi \}) . \quad (17)$$

The parameter γ is the amplitude of the modulation and $\Delta\chi$ the mean optical path difference between the signal and reference beam. With equation (3) it follows that the detected signal for higher harmonics is approximately given by the FOURIER transform of

$$\text{Re} (\mathbb{E}_{\text{nf}}\mathbb{E}_{\text{bg}} + \mathbb{E}_{\text{nf}}\mathbb{E}_{\text{ref}} + \mathbb{E}_{\text{bg}}\mathbb{E}_{\text{ref}}) . \quad (18)$$

The processing of the frequencies is mathematically very demanding so that a derivation is left to reference. [57] It turns out that the signal $U(f)$ and the optical path difference $\Delta\chi$ for the n -th harmonic can be obtained by looking at the adjacent two sidebands.

One advantage of pseudo-heterodyne compared to self-homodyne detection is that the signal is not only increased, but also principally almost background free. In addition, the actual near field amplitude, not only a near field magnitude as in self-homodyne detection, is determined. Nevertheless, pseudo-heterodyne detection also has some disadvantages. For example, the reference arm leads to the introduction of many potential noise sources. Therefore, the detection method is more difficult to perform.

5 Setup

The s-SNOM measurements on all samples were performed with a commercial s-SNOM from Neaspec GmbH. [58] As common for s-SNOM, the microscope is based on an AFM, which was run in amplitude modulation tapping mode. For the near-field measurements, an additional optical assembly was added that is schematically shown in figure 16. The functionalities of the s-SNOM have already been discussed. Nevertheless, it should be mentioned that the setup for a switch between self-homodyne and pseudo-heterodyne detection was not changed, but the reference arm was inhibited or intercalated by the beam block instead. The strength of the reference arm was adjusted using a neutral density filter.

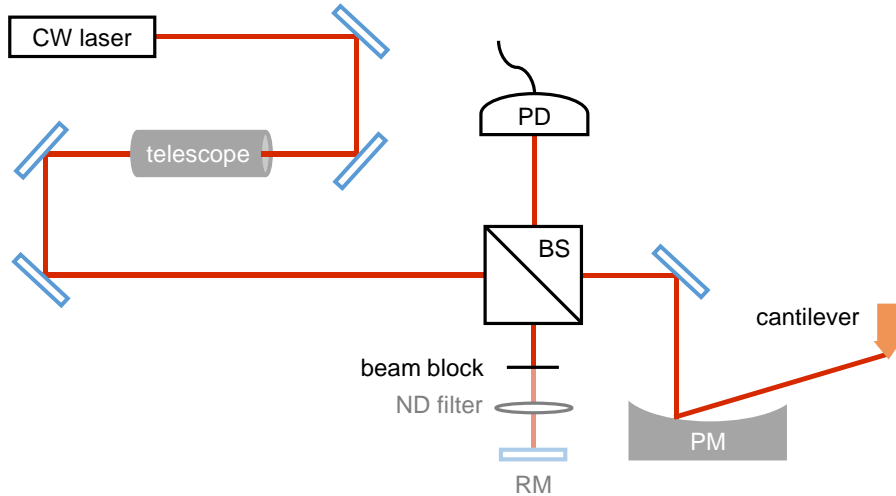


Figure 16: Schematic illustration of the optical setup. The abbreviations stand for: BS - beam splitter; PD – photodiode; ND – neutral density; RM – reference mirror; PM - parabolic mirror.

Working principle of a laser

A brief introduction to the function of a laser is given in the following, because it is the heart of the optical setup. A laser (light amplification by stimulated emission of radiation) is a device to generate a laser beam whose photons are characterized by the same frequency and phase, collectively called coherence. In the simplest case, the medium of a laser represents a three-level system, but usually a multi-level system. The population of states N of a system is given by the BOLTZMANN distribution:

$$\frac{N_j}{N_k} = \frac{g_j}{g_k} \exp\left(-\frac{E_j - E_k}{k_B T}\right). \quad (19)$$

Here, the subscripts j and k denote to a state, k_B is the BOLTZMANN constant and g_j and g_k are the statistical weights of the corresponding energy levels [59], which are assumed to be degenerate in the following.

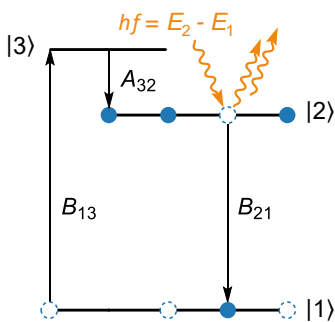


Figure 17: Illustration of the EINSTEIN coefficients using a three-level system.

As an example, a three-level system, as shown in figure 17, is considered. The transition probabilities between the states of the system are described by the EINSTEIN coefficients B_{jk} , B_{kj} and A_{kj} , where j denotes the relaxed state and k the excited state. [60] By induced absorption B_{13} , several electrons are transferred from the ground state $|1\rangle$ into the second excited state $|3\rangle$, which relaxes very quickly without radiation or via spontaneous emission A_{32} into the first excited state $|2\rangle$. It must be achieved that the state $|2\rangle$ is higher populated than $|1\rangle$. This is called population inversion and is a necessary prerequisite for the operation of a laser because the spontaneous emission A_{21} is more probable in the thermodynamic equilibrium. Relaxation to the ground state $|1\rangle$ is thus effected by the stimulated emission B_{21} , which is generated by an

external photon of the energy $hf = E_2 - E_1$. [61] The irradiated and emitted photons are coherent, whereby one of the two photons induces other excited electrons to relax via B_{21} - a chain reaction occurs. The result is the laser beam.

Components of the setup

- **Laser:** There are basically two types of lasers: continuous wave (CW) and pulsed and ultrafast lasers. Two different CW lasers were used for the setup, which can excite the A exciton of 2H WS₂. The first laser is a CW diode laser and the second is a helium-neon (HeNe) laser. It should be noted that the line width is essentially determined by the measuring instrument. An ideal laser has no line width and a constant phase, thus an infinite coherence length. Real lasers have a finite coherence length. A stable interference pattern can only be observed if the coherence length of the photons is greater than the overall difference in path length to the detector. This is especially important for pseudo-heterodyne detection. In the course of this work, the CW diode laser was replaced by a HeNe laser that has a significantly higher coherence length.
- **Telescope:** The telescope was used to focus the laser beam. It was especially necessary for the CW diode laser. Because the focus for the HeNe laser was already excellent, the telescope was removed using this laser.
- **Parabolic Mirror:** The telescope was used to focus the laser beam. It was especially necessary for the CW diode laser. Since the focus for the HeNe laser was already excellent, the telescope was removed using this laser. A parabola can be described by a 2nd-degree polynomial. The rotation produces a rotation paraboloid. Mirrors with that geometric shape are called parabolic mirrors and have the property of collecting incident rays parallel to the axis exactly at their focal point, which makes them very suitable for alignment. Those mirrors also have the advantage of collecting a large part of the scattered light so that no components of the already small near-field signal are lost. For a convenient placement, the tilt of the mirror is adjusted so that the reflected beam is collinear with the incident beam.
- **Photodiode:** Photodiodes are semiconductors that, as a result of the photoeffect, convert incident photons into electrical current or rather into signal voltages.
- **Beam block:** The beam block is responsible for decoupling the reference arm from the setup. To put it simply: If the beam block is present, the measurement is using self-homodyne detection, otherwise the data are acquired in a pseudo-heterodyne manner. For noise-free pseudo-heterodyne detection, the reference arm must be carefully calibrated.

6 Preparation procedure

During this thesis, an effective and reproducible measurement routine was developed that is presented in this chapter.

6.1 Preparations for AFM

The positioning of the probe tip at the beginning of a series of measurements is indispensable.

Placement of the cantilever and resonance curves

For this purpose, the holder mount is removed from the s-SNOM and heated on a heating plate with 90 °C for two minutes. After that, a granule of solid glue is placed on the heating plate by using a tweezer that melts due to the heat. This process is very important for the quality of the resonance curves of the cantilever. While determining the size of the glue granule one should make sure that the size of the melted glue droplet has a slightly smaller diameter than the width of the cantilever holder. Once the melting is done, the rubbing of the glue droplet with the tweezer starts, so that the contact surface of the holder mount is completely covered with glue.

Afterward, the cantilever is placed carefully onto the holder with a tweezer, which is free of glue. If necessary, the position of the cantilever can be adjusted by pushing it with the tweezer, while being cautious to not damage the tip. The holder is then removed from the heating plate and cooled down for at least five minutes. Finally, the holder can be installed back into the s-SNOM. If a cantilever is to be replaced, the procedure is almost identical. However, the old cantilever must be removed first. The holder is then cleaned with a solvent, e.g. isopropanol.

An important indicator of whether the placement process was successful or not is the quality of the resonance curve. It can be picked up after aligning the tracking laser with the cantilever surface. The narrower the curve, the higher the quality factor Q , which also enables the system to be more sensitive regarding changes in the tip-sample-distance z . A symmetrical curve shape provides a similar behavior of the amplitude A_{cant} for both positive and negative distance changes. Adhesive effects usually result in several local maxima in the curve. Care should be taken to ensure that these are well below the setpoint amplitude A_{cant} of the cantilever. However, this is usually the case for curves with a high Q factor.

The excitation voltage U_{tap} is another quantitative indicator of the quality, next to the appearance of the curved shape. This determines the cantilever amplitude as a function of the damping. If a high excitation voltage U_{tap} is required to achieve a certain amplitude A_{cant} , then a lot of energy is lost due to damping. A very good quality factor is achieved when U_{tap} in mV is about half of A_{cant} in nm. The measurement series used driving amplitudes A_{drive} in the range from 50 to 100 nm.

Checking the tip with the TGQ1 test grid

Since damage to the tip can occur while placing the cantilevers or when approaching the sample, the intactness of the tip must be checked. This can be done with the TGQ1 test grid. In addition to that, the calibration of the piezo crystals can be adjusted in all three spatial directions with TGQ1 as well. The sample consists of SiO_2 and Si and has three quadratic levels of different height; the step heights between the levels are 20 nm and 1.4 nm, respectively. Each square has an edge length of 1.5 nm. [62] Figure 18a shows an AFM phase image of TGQ1 with an intact tip and figure 18b the same sample, but with a damaged tip. The damage is noticeable by the doubling of the sample edges. Another indicator for a damaged tip is that the steps are no longer squares, but distorted.

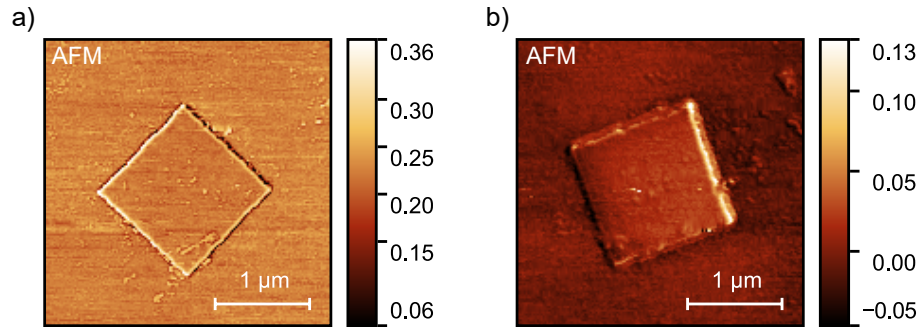


Figure 18: Mechanical phase images of TGQ1 with (a) an intact tip and (b) a damaged tip. The color bar displays angles in rad.

6.2 Preparations for s-SNOM

After ensuring that the resonance curve of the cantilever and the tip are reasonable, the CW laser is turned on. As discussed in chapter 5, optimal laser alignment is essential to obtain a near-field signal.

Searching for the near-field signal

Before the search for the optical signal takes place, it is checked whether the incident light is focused or not. To do this, the z -height of the sample is changed. The laser beam is then moved from the focus point along a diagonal, in a positive or negative direction. An optimal focus is achieved when the diagonal describes an opening angle of about 45 degrees, and the expansion takes place symmetrically in both directions. Otherwise, a refinement of the last two mirrors in the setup is necessary until the discussed is ensured.

When the focus is set, the laser beam is directed at the apex of the tip and the detector signal is evaluated. At this point, homodyne detection is used, meaning that the reference arm is blocked. If a signal is found, it can be maximized in a computer window by optimizing the tip position. In this case, it means that the absolute signal and the signal-to-noise ratio (SNR) are large and, therefore, stable. In particular, it is recommended to consider the third and fourth harmonic so that one can be aware of not aligning into stable scatter – especially in the visible range [63]. However, caution is advised here. A maximum signal does not mean that it is a maximum near field. A stable background signal could be obtained for higher harmonics as well.

The approach curve can prove that the signal found is actual near-field signal. Here, the tip is moved to a defined position of the sample, and, once this is done, the tip-sample distance is increased. Meanwhile, the scatter intensity is measured. If there is a background-free near-field signal, a large scatter intensity can be found at a small tip-sample distance, which drops rapidly in the far-field, see figure 19 (blue curve). This is different in the case of a significant background signal, which also exhibits a contribution part in the near-field and thus falsifies the signal. That is also shown in figure 19 (orange curve).

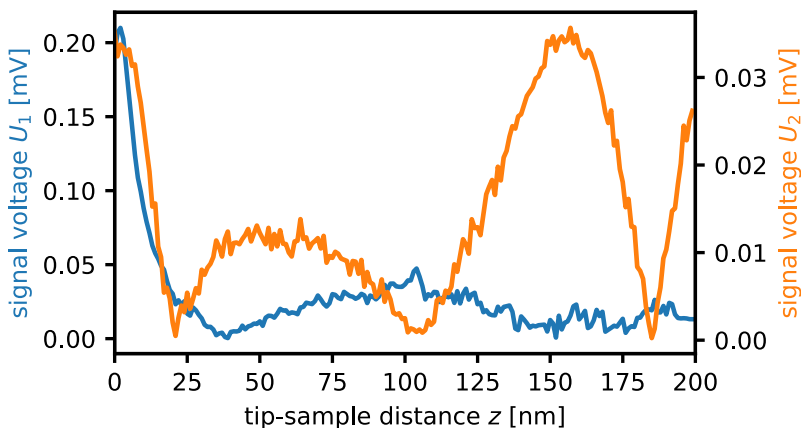


Figure 19: Optical approach-curves (measured in self-homodyne manner) showing the detected signal voltage U ; the blue one contains little background scatter and the orange much.

Another important factor for the quality of an approach curve is noise. Unlike the signal composition, the noise can be estimated very well by the signal-to-noise ratio (SNR). If the SNR is low, the recorded sample images will lose sharpness and sample details may be lost, cf. figure 20b.

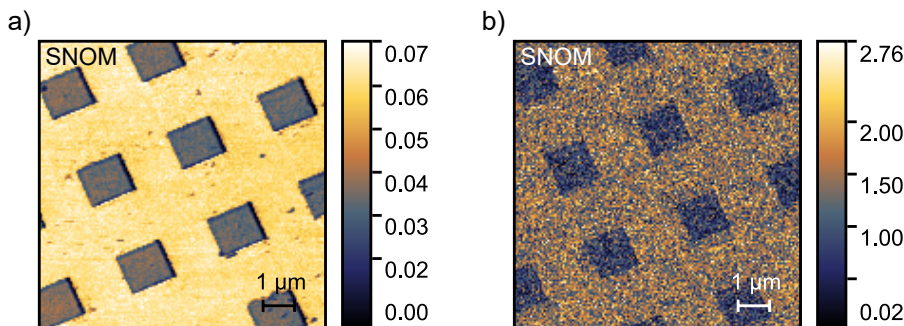


Figure 20: Optical images at the fourth-harmonic demodulation of TGQ1 with (a) a high SNR and (b) a low SNR. The color bar displays voltages in mV.

If the presence of the near-field signal is proven and the SNR is sufficiently large, a test scan with TGQ1 is performed. This ensures the long-term stability of the signal. By changing the position of the tip, new environmental factors, and thus potential sources of interference, are introduced. This can lead to an attenuated signal with increasing scan duration. In the optimum case, the quality of the signal remains constant during the entire scan. If the near field at TGQ1 remains constant, this is unfortunately not sufficient for a durable near field for other – less grateful – samples. In homodyne detection, a fluctuating near-field on Tungstendisulfide was an omnipresent problem.

It can happen that even after a long search, no near-field signal is detected, but only a background signal. In this case, there are two possibilities to continue:

7 Tip performance

- Replacing TGQ1 with a gold sample. The advantage of gold is that it is a plasmonic sample. Plasmons can be classically described as oscillations of free electrons relative to stationary positive ions. [64] Such samples generate a particularly strong tip-sample interaction [65], which makes the signal easier to find. An interpretation of the images of plasmonic samples is difficult because of the more complex interaction. Therefore, in this work, the only aim of using these samples is to find the signal.
- Exchanging the cantilever. Damage to the tip may have occurred, e.g. through the loss of near-field reinforcing tip-layers, which have not yet been observed in the AFM images.

Replacing the Sample

Once a stable near-field signal is found, the test sample can be exchanged and the sample of interest inserted. Because of the changed tip-sample interaction, a shift of the resonance frequency Ω_0 is expected, which is why the resonance curve should be recorded again. If the curve was of good quality, it is going to be reproduced with the new samples.

7 Tip performance

An important finding within the thesis was that different tips are differently suitable for the resolution of certain sample characteristics. These are discussed in the following.

The great advantage of the s-SNOM technology is that it can resolve phenomena below the diffraction limit and obtain in situ morphological, viscoelastic, optical, dielectric and other information about the sample. However, during the investigations on the WS_2 sample, it was found that there is a divergence between the ability of tips to obtain all information about the sample. Different tips of different designs and materials were used, and three proved to be particularly effective.

- platinumiridium (PtIr) tips of the company Nanoworld
- PtIr tips of the company NeaSpec
- gold (Au) tips of the company Opus

While the NanoWorld tips with PtIr coating [66] are particularly suitable for capturing high-resolution AFM images, diametrically, gold-coated tips [67] provide particularly good SNOM images for the WS_2 sample. Neaspec PtIr tips are equipped with a special type of construction that is intended to strengthen the near field. [58] Accordingly, a better near-field signal is achieved with those tips than with NanoWorld tips, but a worse one than with gold tips. Furthermore, AFM images using the Neaspec PtIr tips have the lowest resolution. However, another factor must be taken into account: The stability and thus the longevity. It turns out that both PtIr tips are significantly more stable and durable than gold tips. This applies to the laser power of the SNOM laser as well. The gold coating can only withstand irradiation by a laser beam with low power – otherwise, the coating melts. This, in turn, has consequences for near-field enhancement: the higher the laser power, the stronger the enhancement. However, the quality of the SNOM images using gold tips was superior to that of the NeaSpec PtIr tips, even with lower laser power.

This is an interesting finding, because platinum and gold both have a distinct imaginary part of the dielectric function in the energy range of the A exciton. [68, 69] Stability is also important for topographic imaging and gold-coated tips prove unsuitable for demanding surface topologies. The properties of the tips are summarized in table 1.

Table 1: Overview of the properties of the tips used. Some table elements contain the comparative digits from 1 to 3, with 1 indicating the best and 3 the worst tip.

Company	Material	AFM quality	s-SNOM quality	Stability
NanoWorld	PtIr	1	3	1
NeaSpec	PtIr	3	2	1
Opus	Au	3	1	3

In summary: some tips are more suitable for good AFM and others for good s-SNOM recordings. What does that mean in concrete terms?

The criteria for a good AFM recording are, first of all, a good resonance curve, i.e. a high quality factor Q , as well as a good approach curve and high resolution. This also explains the evaluation within table 1: Although Neaspec tips have the lowest resolution, they are superior to gold tips in the other two aspects. It was particularly noticeable in approach curves that the cantilever amplitude A_{cant} was reproducibly extremely poor for gold tips, as shown in figure 21. The reason for this is probably a strong sulfur-gold interaction. [70]

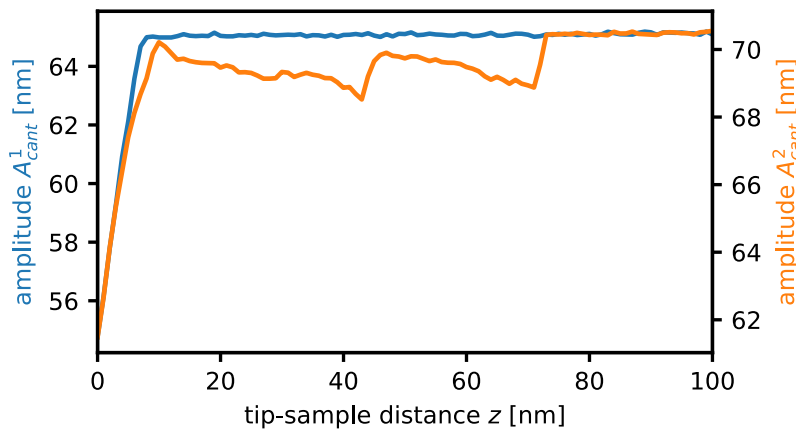


Figure 21: Mechanical approach curves showing the cantilever amplitude. The blue graph A_{cant}^1 refers to a PtIr tip and the orange one A_{cant}^2 to a gold tip.

Meaningful s-SNOM recordings are characterized by high signal strength and low background, which can also be frugally checked by approach curves.

In some cases, this divergence to gain good optical and topographic information simultaneously may result that certain information can not be recorded in situ. For example, using gold tips, the mechanical

7 *Tip performance*

phase-contrast sometimes is so low that it was no longer possible to capture certain sample properties. On the other hand, using Nanoworld PtIr tips, it was hardly possible – at least for the WS₂ sample – to find any near-field signal at all. As a consequence in this thesis, in some instances phenomena had to be examined one after the other with different tips. Although the NeaSepec PtIr tips offer a balance between topological and optical image quality, Nanoworld PtIr tips were mostly used for pure AFM images and gold tips for near-field mapping.

Part IV

Results and discussion

The work achieved results in two different areas in particular. One is related to the evaluation of the investigated systems – 2H WS₂ and terrylene – and the other to the refinement of the optical setup. In the following, it is demonstrated that lateral spectroscopy can contribute to answering open questions regarding intriguing systems. In addition, it is shown that an improvement in the experimental setup can open the way to deeper insights. Finally, on the basis of the knowledge gained, an outlook is given as to which modifications can be introduced in the future.

8 Spatial inhomogeneity in few-layered WS₂

A WS₂ flake, directly deposited on SiO₂ via CVD, was examined. According to the manufacturer, these are monolayers of the 2H phase. The sample has already been characterized by S. CALATI using reflection contrast spectroscopy (RCS), with results that are difficult to interpret.

With RCS, a reflection spectrum can be determined as a function of the wavelength or energy of the incident light. It is isomorphic to an absorption spectrum and allows conclusions about the complex part of the dielectric function $\text{Im}(\epsilon_{\text{sample}})$ and electron densities in the conduction band. [71] The reflection contrast RC is determined by the following equation [38]:

$$\text{RC} = \frac{R_{\text{sample}} - R_{\text{substrate}}}{R_{\text{substrate}}}. \quad (20)$$

Here, R_j is the degree of reflection of the sample or substrate. Figure 22 shows an optical microscopy image of the sample. Triangular-shaped elements are visible; they are the WS₂ flakes on the substrate.

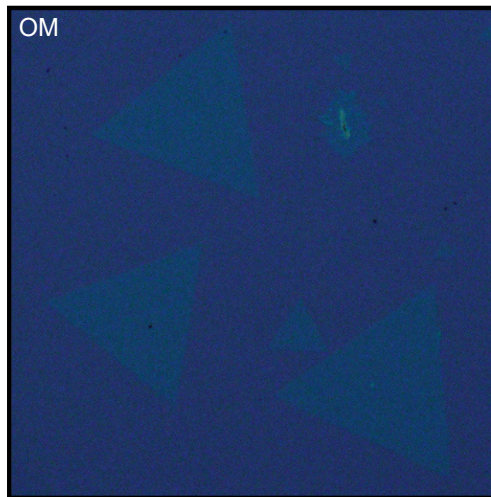


Figure 22: Optical image of a homogeneous WS₂ triangle.

A particularly large WS_2 flake with an edge length of about $200\ \mu\text{m}$ was selected by an optical microscope. When viewed with this microscope, it looks as if the flake is a homogeneous species. As discussed later, this is not the case on few micrometer to nanometer length scales. On the basis of this apparent homogeneity, a series of reflection contrast measurements in the energy regime near the A exciton resonance were performed. As shown in figure 23, these experiments yielded very different reflection contrast spectra. The main resonance is shifted by up to 40 meV and the peak shape changes.

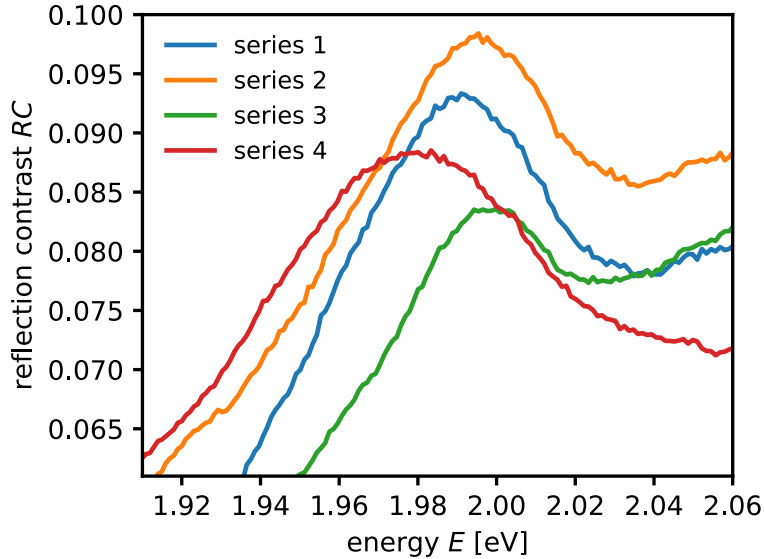


Figure 23: Reflection spectra of different measurement series for the same WS_2 flake. The measurement data were received from S. CALATI.

Optical microscopy of the investigated flake with a higher resolution was performed to elucidate the origin of these differing results. The optical image in figure 24 shows irregularities. The center, the edges and the center-corner junction are darker compared to the rest of the flake.

Although the optical microscope can resolve the inhomogeneities, however, it is not enabling a more in-depth evaluation. In order to analyze how those inhomogeneities arise, AFM was used. Topographic ranges greater than $50\ \mu\text{m}$ were scanned with a PtIr tip in tapping mode, resolving the optical inhomogeneities in the topography as well. The AFM data were compared with the microscopic image. For this purpose, cross-sections of the topography along the dotted path, cf. figure 24, were considered. It should be noted that the paths are for orientation purposes only; they are not scaled.

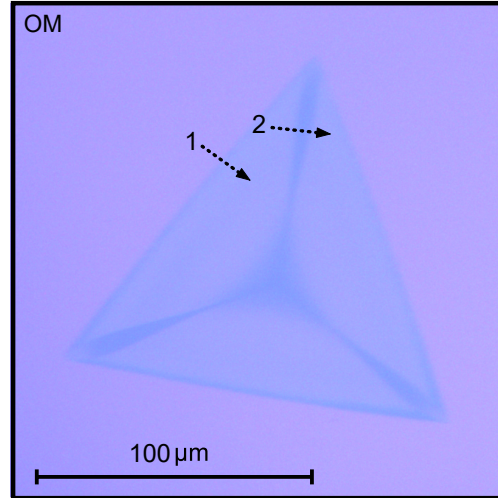


Figure 24: Optical image of the WS₂ flake with an optical microscope that can resolve the spatial inhomogeneities.

Figure 25 shows the height cross-section along path 1, which is orthogonal to the substrate-triangle edge. The apparent height h_{ap} is of little significance here, as the acquisition was acquired over a large area. A background can be created by piezoelectric effects. Theoretically, it can be removed by subsequent processing, but the danger of manipulating measurement data is that meaningful data can also be eliminated. For the determination of the layer thickness, only the relative height difference Δh is of interest only. Therefore, a sigmoid fit function according to BOLTZMANN was calculated. As a result, the height difference of the substrate-sample edge is estimated at $\Delta h \simeq 2.3$ nm. A comparison with the literature [72] shows that this value corresponds to a trilayer ($\Delta h_{lit}^{mono} \simeq 0.9$ nm, $\Delta h_{lit}^{bi} \simeq 1.7$ nm, $\Delta h_{lit}^{tri} \simeq 2.5$ nm).

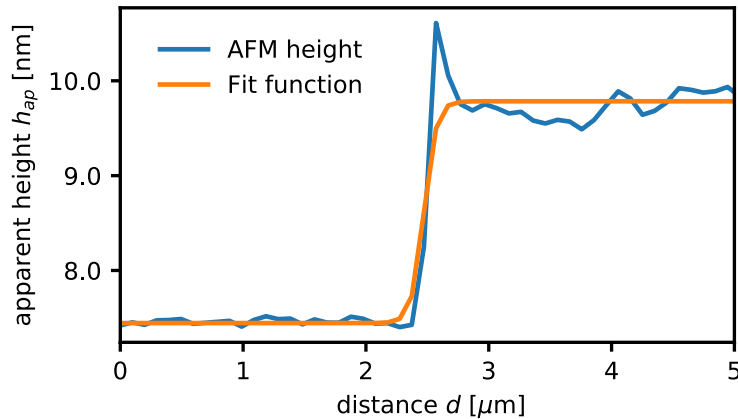


Figure 25: Cross-section of the topography (blue) and the corresponding fit function according to BOLTZMANN (orange).

In addition, the topography along path 2 in figure 24 was measured. The apparent height h_{ap} is shown in figure 26 and has changed due to the piezo creep mentioned above. The relative step height difference is

$\Delta h \simeq 1.2$ nm, meaning that the flake height at the darker areas is approximately 1.1 nm. A comparison with the literature intends that it is a monolayer. [72]

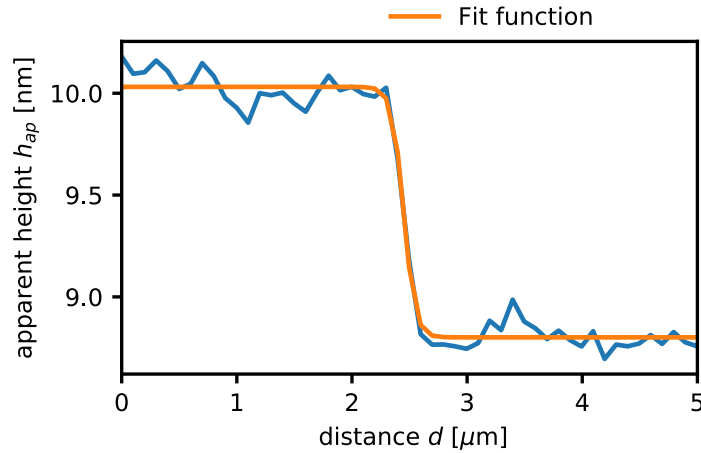


Figure 26: Cross-section of the topography (blue) and the corresponding fit function according to BOLTZMANN (orange).

Nevertheless, the relative height difference measurements should be interpreted carefully. If the height of the monolayer is overestimated compared to the literature, the same should apply to the height difference of the substrate-sample edge. However, the height of the supposed trilayer is below the literature value. Furthermore, there is an instantaneous depression to the monolayer at the edge. This are indications that elevated topography does not describe a trilayer but a bilayer.

The different morphological structures within the flake can explain the shifts of the A exciton: The flake was irradiated with a white light laser. Because the beam radius is large and could not always be placed exactly in the same position, dissimilar areas of the sample were considered for different measurements. This is illustrated for three different measurements in figure 27.

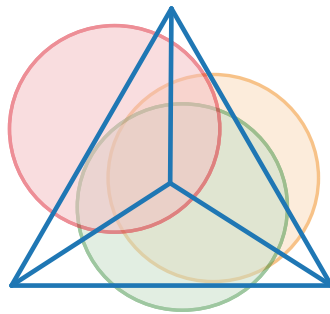


Figure 27: Schematic illustration of the cause for the shift of the A exciton in the reflection spectra.

Summary

In this chapter, the power of SPM was illustrated using the example of AFM. Phenomena could be clarified that were not accessible with conventional microscopy. Spatial irregularities have been resolved on the microscopic length scale. The question arises as to how the nanoscopic composition of the sample is and if there are still inhomogeneities to be found.

9 Topography and optical nanoscopy of WS₂

In this chapter, SPM methods are used to resolve and interpret nanoscopic phenomena. Although AFM provides topological and structural information, s-SNOM images provide a nanoscale map of chemical composition and dielectric interactions, both below the diffraction limit. A combination of both techniques reveals casual contexts of topography, phase-contrast and near-field enhancement.

9.1 Spatial correlation of topography and self-homodyne detection

A section of the flake tip, as discussed in the previous chapter, was examined, see figure 28a. It should be noted that the circled area is for orientation only and not scaled. For the measurements, a gold tip was run in tapping mode. The tip was illuminated by a diode CW laser with a wavelength of approximately 640 nm. The scattered light was detected in self-homodyne manner. Figure 28 also shows (b) the topography, (c) the near-field magnitude demodulated at the third harmonic and (d) the mechanical phase, which were all measured in situ. The scan area has a size of $2 \times 2 \mu\text{m}$ and 100×100 pixels so that the transversal resolution is about 20 nm, clearly in the subdiffraction area.

The topography in figure 28b shows a seemingly homogeneous background, namely the substrate, onto which the WS₂ sample was deposited. The tip of the otherwise triangular flake is missing and a hole in the substrate is visible above it. The flake does not only show inhomogeneities on the microscopic scale (see chapter 8) but also on a nanoscopic level. There are many small granules distributed over the entire flake. The edges show a clear increased height and granule concentration compared to the inner part of the flake, which is shaped by fluctuations. Remarkably, the optical signal in figure 28c reproduces many characteristics observed in the topography. Although the phase-contrast in figure 28d shows the contours of the flake as well, it still is too low to obtain additional information.

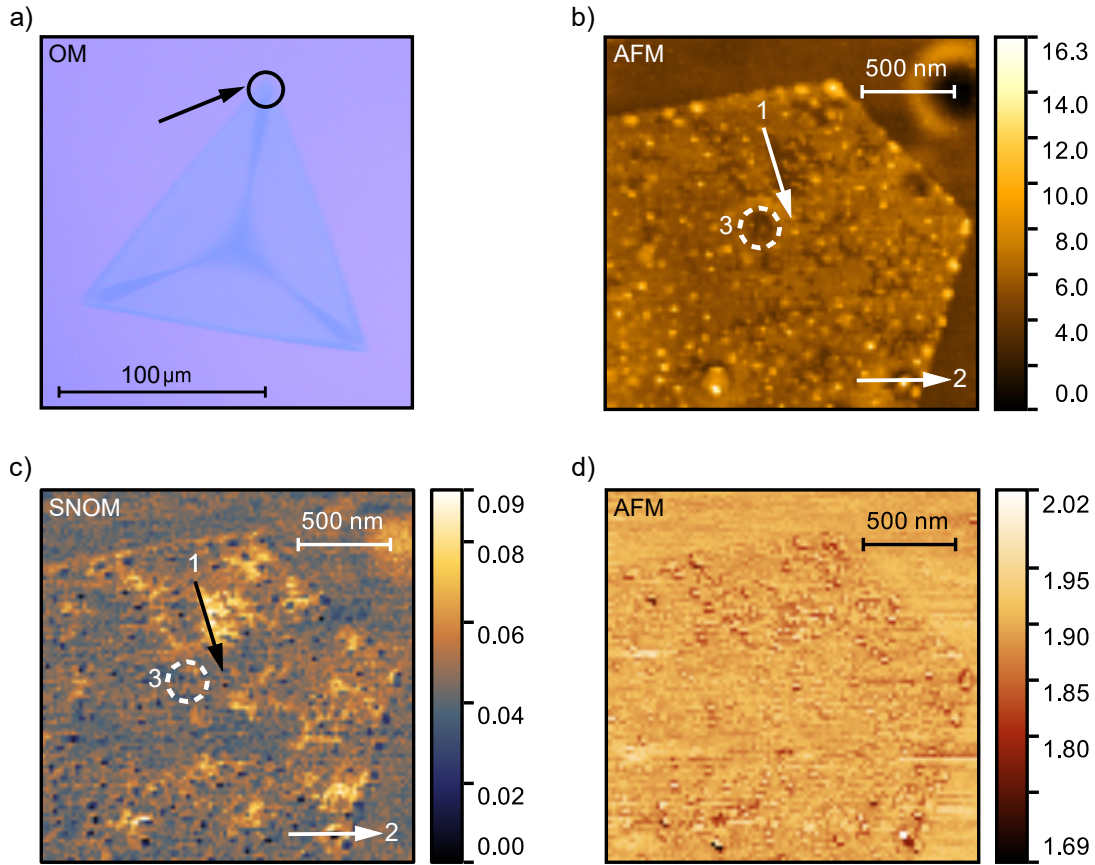


Figure 28: (a) Optical image of the WS_2 flake; (b) Topography image of WS_2/SiO_2 . The color bar displays the apparent height in nm; (c) Optical image of WS_2/SiO_2 at the third-harmonic demodulation. The color bar displays voltages in mV; (d) Mechanical phase image of WS_2/SiO_2 . The color bar displays angles in rad.

Qualitatively, it seems as though the topography is anticorrelated to the optical signal to a certain extent: The deep-lying points in the surface morphology are accompanied by an increased near-field scattering magnitude. Cross-sections through the topography show that mono- and few-layered regions are present.

The anticorrelation that was found is quantitatively highlighted in figure 29. There, the apparent height h_{ap} and the optical signal voltage U are considered along the selected paths 1 and 2 shown in figure 28b and c, both of length $d = 500$ nm. Nevertheless, a closer look reveals that the anticorrelation between the topography and the optical signal is not isomorphic. In figure 28b and c, area 3 shows a noticeable depression in the topography, but only minor changes in the optical signal.

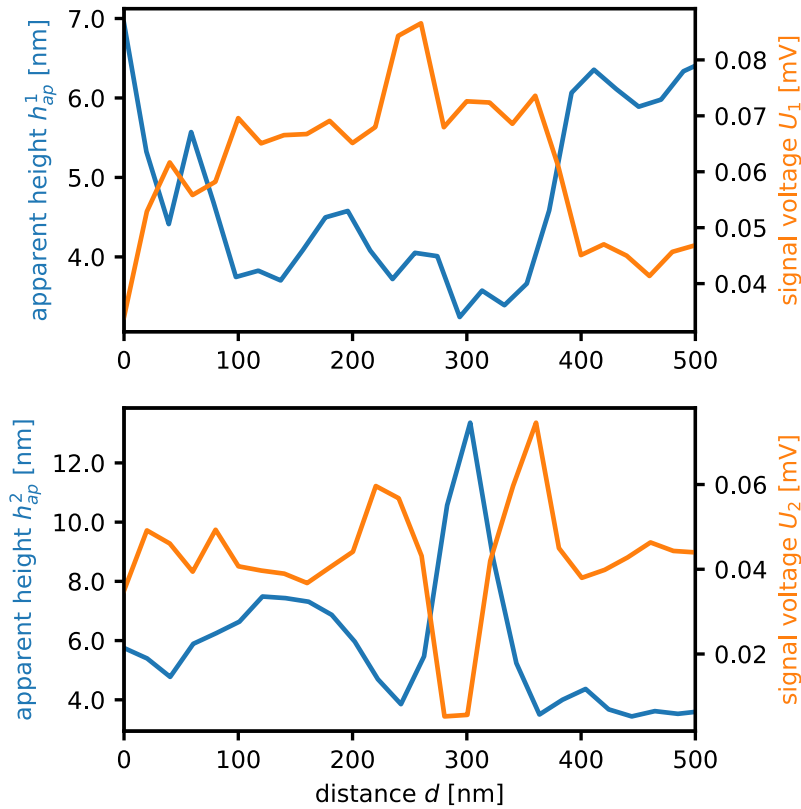


Figure 29: (a, b) Cross-sections of the topography (blue) and near-field magnitude (orange) along the paths 1 and 2, respectively.

Because of the low mechanical phase-contrast with the gold tip, the identical flake area was also examined ex situ using a PtIr tip. The scanning range is $2 \times 2 \mu\text{m}$ again with a transversal resolution of 20 nm. The mechanical phase difference is plotted in figure 30 and displays a significantly higher contrast due to the intrinsically higher quality factor Q of the tips.

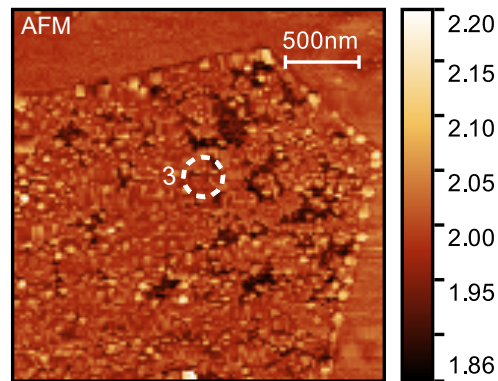


Figure 30: Mechanical phase images of WS₂/SiO₂. The color bar displays angles in rad.

The phase image now reveals dark spots that are not present in the phase image acquired by a gold tip, cf. figure 28d. A comparison with the near-field magnitude shows that the lower the mechanical phase, the higher the optical signal. Strikingly, it seems that, unlike in topography, all features are isomorphic to the optical signal. The marked area 3 is the same as in figure 28b and c. It shows hardly any contrast in the mechanical phase, as there is almost no near field contrast in the optical signal. The phase information, therefore, provides additional information that was not available in the topography. This analysis indicates that the enhancement of the near field magnitude is not only due to a change in the effective distance between tip and sample but also due to nanoscopic changes in the optical properties.

Interpretation of the Results

In summary, an anticorrelation between topology and near-field scattering magnitude was found that contains a significant discrepancy. In this aspect, the mechanical phase shows good agreement with the optical signal. Two hypotheses were developed to explain this phenomenon.

i) Although WS₂ samples, which are exclusively present in the 2H phase, have already been produced, CVD defects can occur during sample preparation. Under certain growth conditions, it is possible that meshed WS₂ structures of the allotropes 2H, 1T and 1T' form. Here, the 1T and 1T' phases are embedded in the 2H matrix. The metallic 1T or 1T' phase may be responsible for the near-field magnitude amplification. The packing of the atoms would have to be studied by scanning tunneling microscopy (STM) images, which allow resolutions in the subatomic range, to test this hypothesis. However, this hypothesis is not supported by the fact that these alternative phase structures are usually only a few nanometers in size [73], whereas the areas of high phase-contrast can be several hundred nanometers large.

ii) The areas with high near-field magnitude are monolayers. The change of the optical properties is due to the easy manipulation of the dielectric function of monolayers. Because of the pronounced electrostatic tip-monolayer interaction, a distinctive additional interaction may occur. Using some technical assumptions, the force in dependency of the tip-sample distance can be described by

$$F_{ts}(z) = \frac{A_H R_{tip}}{6z^2}, \quad (21)$$

where R_{tip} is the radius of curvature of the tip and A_H the HAMAKER constant. The following expression for A_H is derived using quantum field theory:

$$A_H = \frac{3k_B T}{4} \left(\frac{\epsilon_{sample} - \epsilon_{medium}}{\epsilon_{sample} + \epsilon_{medium}} \right) \left(\frac{\epsilon_{substrate} - \epsilon_{medium}}{\epsilon_{substrate} + \epsilon_{medium}} \right) + \frac{3\hbar f_e}{8\sqrt{2}} \left[\frac{(\rho_{sample}^2 - \rho_{medium}^2)(\rho_{substrate}^2 - \rho_{medium}^2)}{\sqrt{(\rho_{sample}^2 + \rho_{medium}^2)(\rho_{substrate}^2 + \rho_{medium}^2)} \left\{ \sqrt{(\rho_{sample}^2 + \rho_{medium}^2)} + \sqrt{(\rho_{substrate}^2 + \rho_{medium}^2)} \right\}} \right]. \quad (22)$$

Here, \hbar is PLANCK's constant, f_e the principal electronic absorption frequency, ρ_j are the indices of refraction and ϵ_{medium} is the dielectric function of the immersion medium. [8] With equation (22) it becomes self-evident that the involved dielectric functions have an influence on the effective tip-sample

force $F_{ts}(z)$. As long as this tip undergoes a strong near-field interaction with the monolayers, an additional force component on the tip is generated. During the interaction, a constant phase shift is induced and becomes apparent in the altered phase-contrast; hence, the change in the optical properties is also detected with an AFM technique. The discussed area 3 of depression in topology might not be a monolayer, but a multilayer that lies within a small cavity of the irregular substrate. Since the monolayer-tip interaction is not present, there is no phase-contrast and no increase in the optical signal, although the sole consideration of the topography would intend this.

9.2 Comparison of self-homodyne and pseudo-heterodyne detection

In the previous section, a self-homodyne study was undertaken. However, spatially dependent background scatter cannot be excluded in self-homodyne detection. The setup was extended in such a way that optical measurement using pseudo-heterodyne detection was also feasible to ensure that the local near-field signal is actually generated by the substrate properties. As will be discussed later, this is necessary to eliminate background contamination.

Achieving a higher harmonic optical signal using pseudo-heterodyne detection was not a triviality. The experimental setup had to be carefully designed to eliminate noise sources. The telescope was dismantled because the laser already has a very good focus. In comparison to self-homodyne detection, the reference arm was unblocked and the interferometer adjusted.

After the optimization of the reference arm using the reference sample TGQ1, the same flake tip as in section 9.1 has been examined using a HeNe laser with a wavelength of approximately 633 nm. A gold tip in tapping mode was still used, but the scattered light was detected in a pseudo-heterodyne manner. In figure 31, the optical recording using pseudo-heterodyne detection (b) is compared to the self-homodyne image (a). All measurement parameters (scan area: $2 \times 2 \mu\text{m}$, 100×100 pixels) are identical.

In pseudo-heterodyne detection b, the flake stands out from the substrate and reveals spatial irregularities, too. Although the self-homodyne image in panel a is less sharp compared to that in panel b, it is noticeable that the areas of high signal voltage for the WS₂ flake are the same in both images. It seems as if a high near-field magnitude is similar to a higher near-field amplitude. However, a conspicuous feature becomes apparent: the cavity in pseudo-heterodyne detection (b) is absent in self-homodyne detection (a). It can be concluded that holes in the substrate are not visible in pseudo-heterodyne detection.

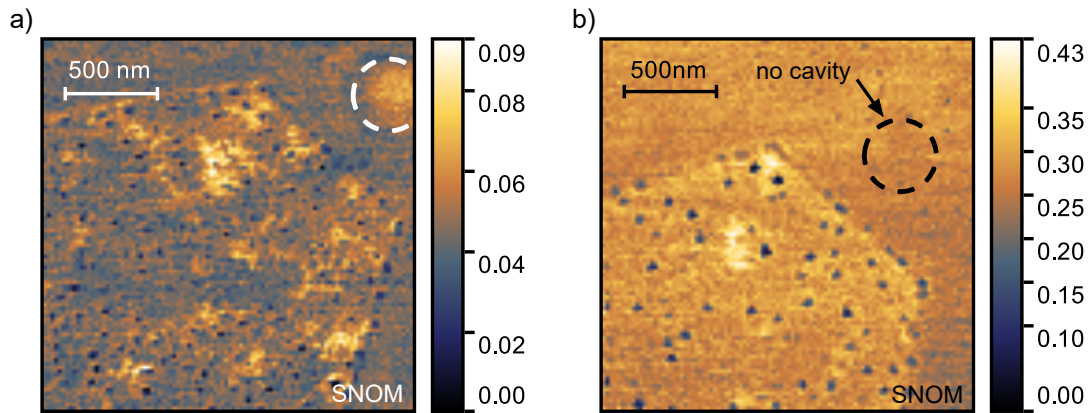


Figure 31: Optical images of WS₂/SiO₂ using (a) self-homodyne detection at the third-harmonic demodulation and (b) pseudo-heterodyne detection at the fourth-harmonic demodulation. The color bar displays voltages in mV.

Why does the topology of the data acquired with self-homodyne and pseudo-heterodyne detection differ? The amplification by the reference arm allows a significantly larger near-field signal, as shown in the approach curve in figure 32.

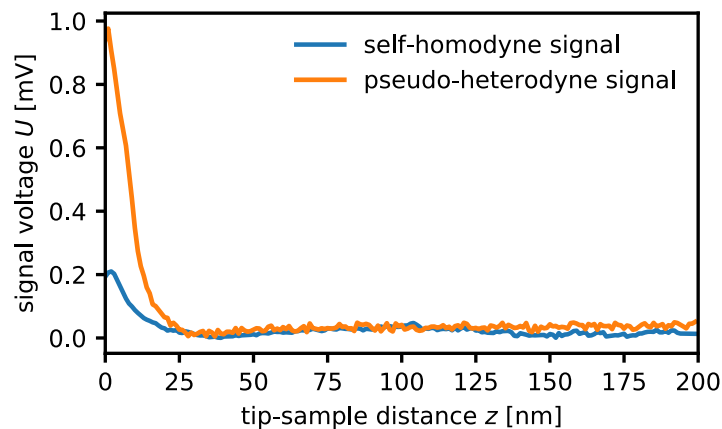


Figure 32: Optical approach curves showing the detected signal voltage U for self-homodyne (blue) and pseudo-heterodyne (orange) detection.

Because the background is better suppressed in the pseudo-heterodyne detection, this indicates that the mapping of the cavity in self-homodyne detection is due to far-field scattering, which contaminates the signal. This can be explained by the fact that there are more scattering possibilities in a cavity, meaning the background portion of the signal is correspondingly large – even in higher harmonics.

In the following, it will be quantitatively discussed why the two methods deliver different sharp images. The signal voltage for the fourth harmonic in pseudo-heterodyne detection is several times greater than the third harmonic in self-homodyne detection, cf. color bar in figure 32. However, the SNR is decisive for the image quality.

Figure 33 shows the normalized median derivation (NMD) of the near-field signal along a homogeneous 2 nm long path on the substrate, each from figure 31. The blue graph represents the path in the self-homodyne and the orange one a path in the pseudo-heterodyne image. The comparison shows that the NMD for pseudo-heterodyne detection is smaller than for self-homodyne detection, whereby a smaller deviation means a better SNR; note that this is a comparison of the fourth (pseudo-heterodyne) and third (self-homodyne) harmonic.

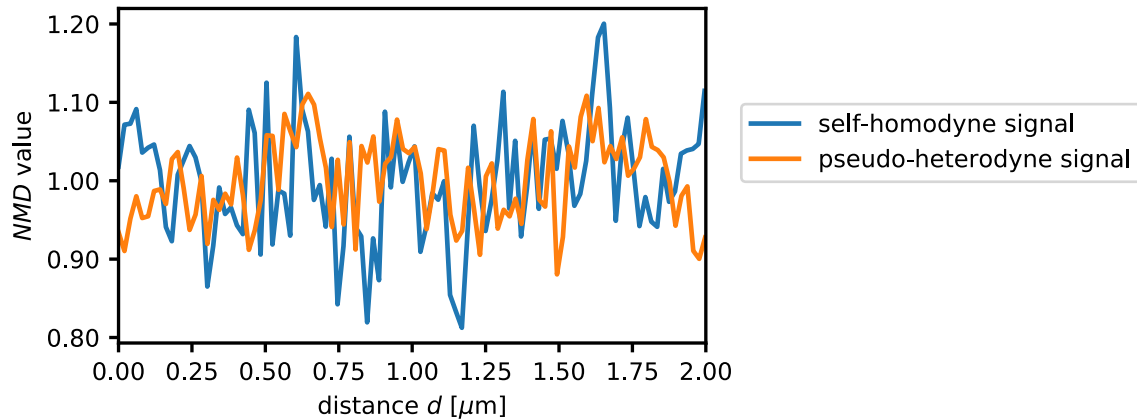


Figure 33: NMD of the near-field magnitude (blue) and near-field amplitude (orange) along a homogeneous 2 nm path on SiO_2 .

It should be noted that the NMD does not make statements about the absolute noise, but only about the relative noise (the SNR). The absolute noise in pseudo-heterodyne detection was still about twice as large as that for self-homodyne detection – but the size and composition of the signals were very different, as discussed in figure 31. This explains why the pseudo-heterodyne image in figure 31a looks clearer: it is due to the higher SNR.

Summary

In this section, self-homodyne and pseudo-heterodyne detection were compared. The noise in pseudo-heterodyne detection was reduced to about the self-homodyne level by using a HeNe laser and carefully adjusting the reference arm. It was demonstrated that the self-homodyne technique contains spatially dependent background scatter, which can be removed by using pseudo-heterodyne detection. This study confirms that pseudo-heterodyne detection is a further developed interferometric technique compared to self-homodyne detection.

9.3 Spatial correlation of topography and the spectral near-field amplitude

Subsequently, this section sits one on top of the others, scrutinising the same flake tip from sections 9.1 and 9.2. For this purpose, ultra-resolved in situ mappings of the topography, mechanical phase difference and optical signal were used.

Because of the excellent near-field amplitudes, higher resolution and more reliable s-SNOM examinations were performed in pseudo-heterodyne manner with a gold tip in tapping mode. A range of 500×500 nm of the discussed flake tip, which is boxed in figure 34a, was examined with a resolution of 100×100 pixels, which corresponds to a theoretical transversal resolution of 5 nm. This is of course limited by the tip radius, but due to the good sampling, extremely clear images were obtained, which are shown in figure 34b–d. The near-field amplitude (b) shows an enhanced area as well as granular depressions of the amplitude. The rest of the signal remains relatively homogeneous. The mechanical phase difference (d) reveals, in addition to the grains, weakly discernible structures.

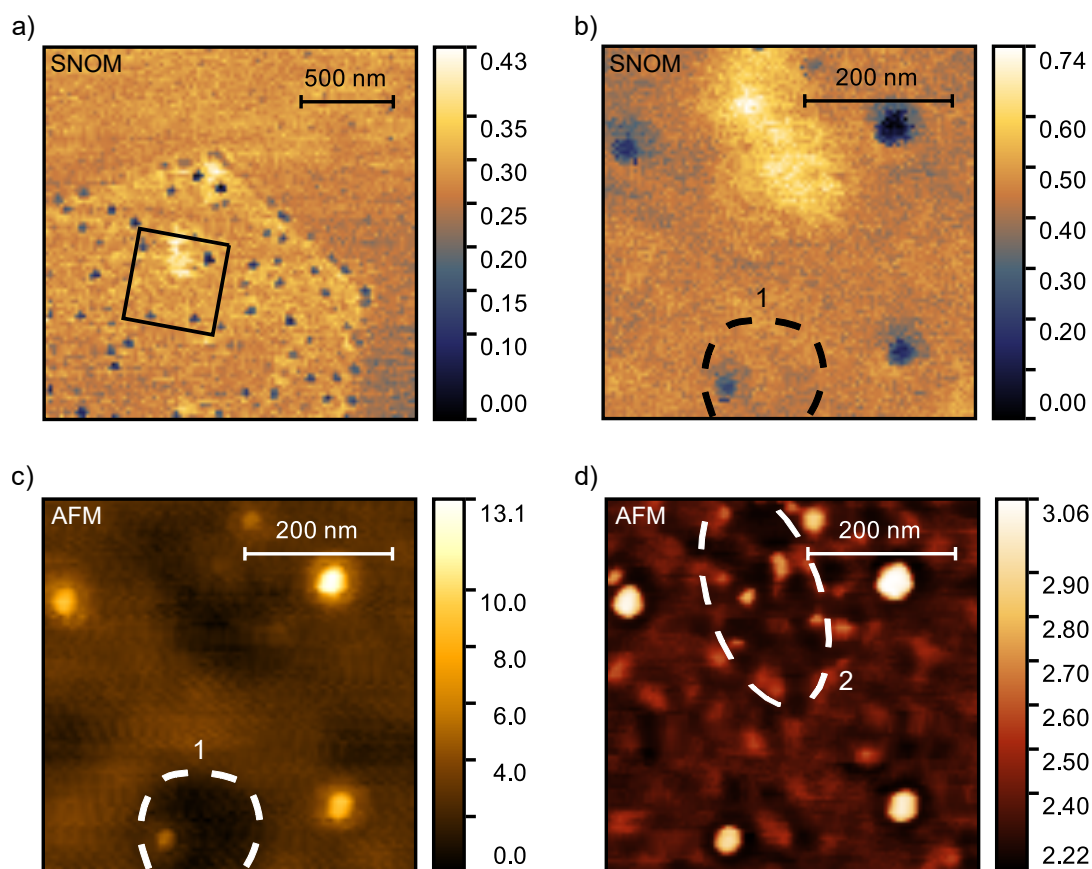


Figure 34: (a) Optical image of WS₂/SiO₂ at the fourth-harmonic demodulation. The color bar displays voltages in mV; (b) Optical image of WS₂ at the fourth-harmonic demodulation. The color bar displays voltages in mV; (c) Topography image of WS₂. The color bar displays the apparent height in nm; (d) Mechanical phase image of WS₂. The color bar displays angles in rad.

A qualitative comparison of the images shows that the corresponding topography (c) does not fully reflect the optical topology (b), as already proofed in the previous section. Remarkably, there are a number of depressions in the lower half of the topography (c) that are not visible in the optical image (b). The marked area 1 in (b) and (c) is particularly prominent.

The resolution of a topology by the mechanical phase difference (d) is surprising because a gold tip was used. The contrast could be the result of good sampling. Interestingly, it reflects the grains and the abrupt

change of the topography (c), especially the edges to depressions. The latter is because the mechanical phase difference also depends on the tip-substrate contact area. The marked area of the mechanical phase (d) corresponds to the amplified area of the near field amplitude (b). It is conspicuous that area 2 in the mechanical phase (d) not only displays the periphery of the optical signal (b) and the topography (c), but also shows an inner, although weak, phase-contrast. This finding supports hypothesis (ii) from section 9.1.

Summary

In this section, ultra-resolved morphological, mechanical and optical images were recorded and compared in situ for the first time in this work. Hypothesis (ii) presented in section 9.1 is also a satisfactory explanation of the findings.

Conclusion for chapter 9

The examined WS_2 sample represents a mix of different layers. Some depressions of the topography show clear optical signals, others not. The apparent height h_{ap} found in the topography does not reflect the actual layer thickness of the WS_2 flakes, but substrate fluctuations are also measured. WS_2 monolayers produce a very pronounced optical near-field amplitude compared to layered films. The near-field amplitude can be accurately recorded by pseudo-heterodyne detection but not by self-homodyne detection. Topographic images that suggest a monolayer but do not show an enhanced optical signal are presumably produced by unevenness in the substrate. These considerations are supported by measurements of the mechanical phase. These observations are summarized exemplarily in figure 35.

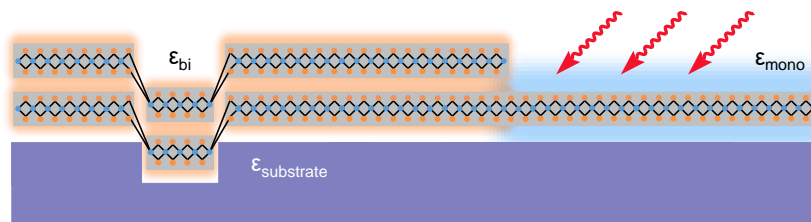


Figure 35: Illustration of the findings in this chapter.

10 Defects

The examined WS_2 flake from the previous chapter was a defective sample. The question of whether other flakes also show similar mixtures of different layers or whether the substrate equally shows defects, is investigated here. This is an important concern, because the electronic properties depend on the morphology of the flakes and to a large extent on the quality of the sample. With this as motivation, SPM studies were performed to find a suitable flake.

10.1 Characterization of sample defects

The answer to how homogeneous a WS₂ flake is determines its applicability in hybrid systems. For the analysis of atomically thin WS₂ layers for heterostructured systems or hybrid systems, primarily defect-free samples and substrates are of interest. This chapter deals with defects that may occur during the CVD growth process.

First, it should be mentioned that defects in solids are intrinsic and unavoidable because they provide entropy gain according to the GIBBS-HELMHOLTZ equation, as shown in figure 36.

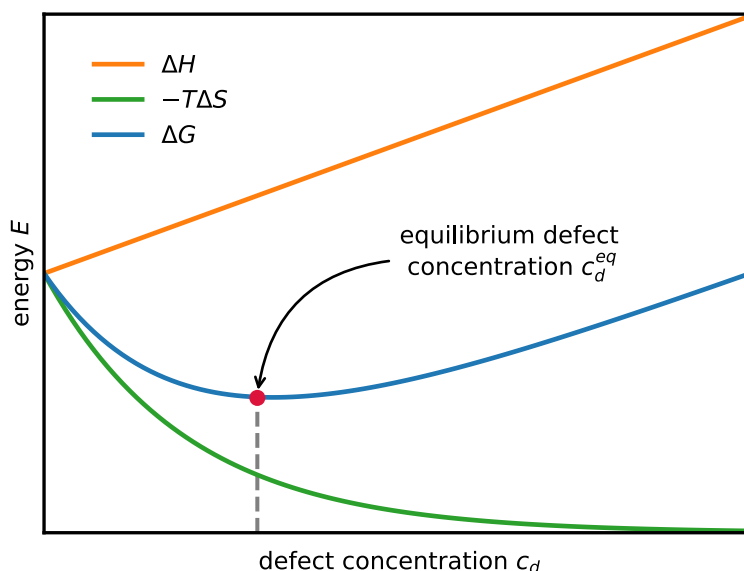


Figure 36: Schematic illustration of equilibrium defect concentration c_d^{eq} according to the GIBBS-HELMHOLTZ equation.

Defects will be caused by the growth process in CVD. In addition, it is known that CVD growth is sensitive to the dynamics of the local chemical environment. [74] This can lead to an accumulation of defective flakes. During the research of the WS₂ triangles, defects occurred particularly frequently in the middle. The larger the flake, the greater the probability of defects, leading to inhomogeneous structures.

WS₂ flakes of different sizes were examined by AFM. Figure 37 displays the mechanical phase difference for three selected WS₂ triangles, which all have a different size and morphology. The size of the examined flakes decreases from image (a) to (c), where (a) and (b) show the center and (c) the entire flake. The scan area has a size of (a) 1.5×1.5, (b) 1×1 and (c) 10×10 μm , so that the theoretical resolution is about 10 nm, which is limited by the tip radius. A PtIr tip in tapping mode was used to acquire the pictures. Panel a shows the fusion of several multilayers that have grown in different directions and therefore show a strong aggregation. This defect can also be detected with a light microscope. The point defect in figure 36b within a monolayer cannot be resolved by such a microscope. The step height measurement of about 1 nm confirms that it is a monolayer. It is striking that the grains, which are omnipresent in all flakes, do not have a random structure, but form a triangular motif. The flake in image (c) is also a monolayer but

without large defects. Unlike in (b), the inner grains have a random structure. The edges of the flakes, as with all the investigated flakes, show a significantly increased grain concentration.

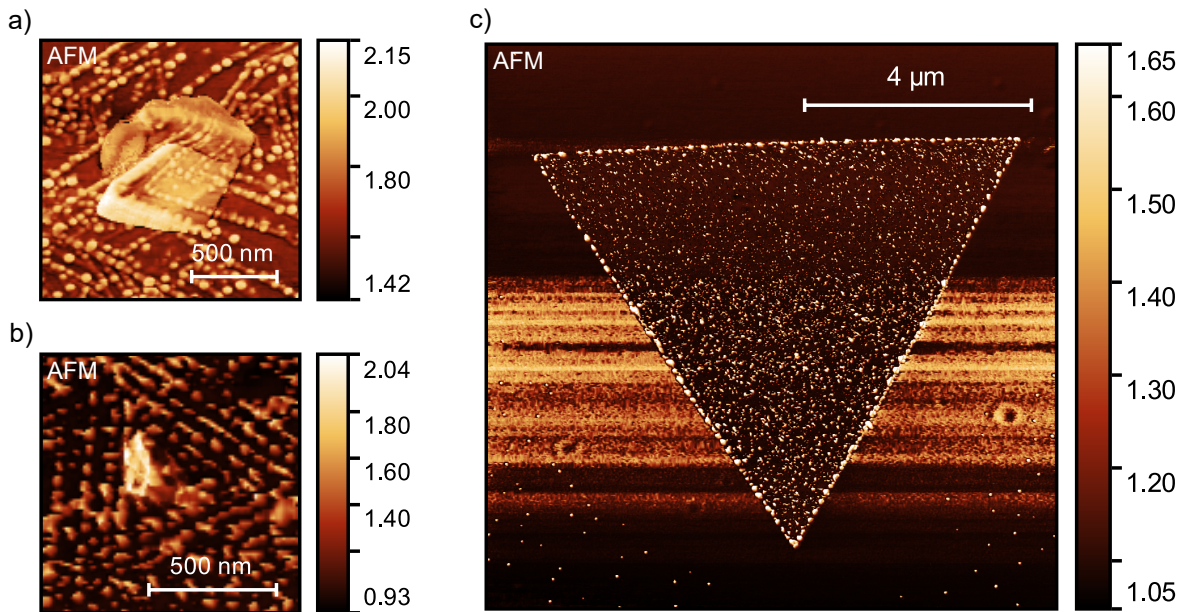


Figure 37: (a, b) Mechanical phase images of defects in WS₂; (c) Mechanical phase image of a low-defect WS₂ flake, including SiO₂. All color bars display angles in rad.

Summary

In summary, defects were characterized in CVD grown, few-layered WS₂ flakes. It was shown that AFM is an important tool for the identification of high-quality flakes for further applications. The AFM experiments showed that the production of large, ultra-thin TMDCs by CVD is possible, but that defect formation cannot yet be completely avoided. Sample preparation by CVD is a current research topic. [75]

10.2 Influence of substrate defects on dielectric properties

In addition to the shape of the flakes, the substrate structure also has an influence on the topology of the topography. It seems though that this does not apply to the mapping of the near-field amplitude. However, is it possible that the substrate also has an effect on the latter?

In the following, a defect WS₂ flake, which has a small size, was examined using s-SNOM. A gold tip in tapping mode was illuminated by a HeNe laser with a wavelength of approximately 633 nm and the scattered light was detected in a pseudo-heterodyne manner. Figure 38 shows an edge of this flake; in (a), the topography and in (b), the near-field amplitude is shown. An area of 3×3 μm size was scanned using 150×150 pixels, meaning that the transversal resolution is 20 nm. In the topography (a), the substrate-sample edge is clearly visible. There are several depressions in the substrate and inside the flake as well as a heightening to which an arrow points. The near-field amplitude in (b) shows the substrate-flake edge,

as well. It is noticeable that the substrate-sample contrast is much higher compared to the images from chapter 9. Moreover, the edge shows a depression of the near-field enhancement.

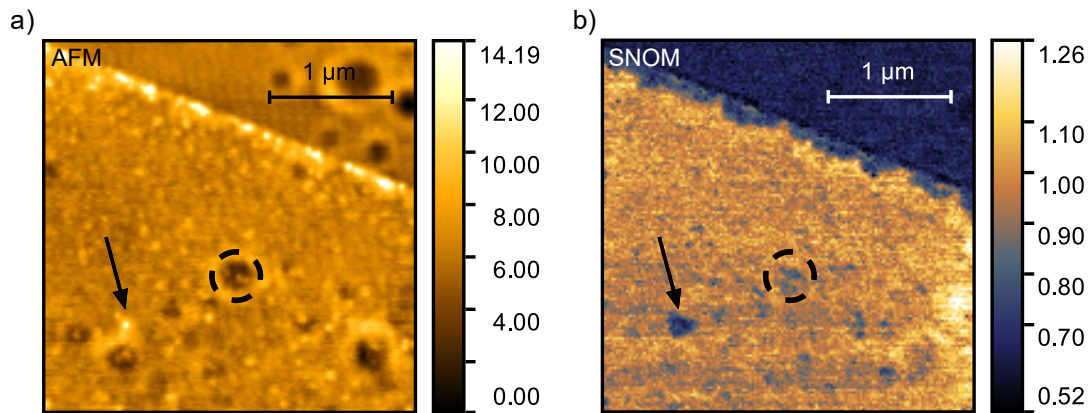


Figure 38: (a) Topography image of WS_2/SiO_2 . The color bar displays the apparent height in nm; (b) Optical image of WS_2/SiO_2 at the fourth-harmonic demodulation. The color bar displays voltages in mV.

Step-height measurements of the substrate-flake edge reveal that the considered WS_2 flake is a monolayer. This also explains why the substrate-sample contrast in the optical image (b) is very pronounced. A drop in near-field interaction is also observed at the edges that are particularly exposed to defects. This was not apparent in chapter 9, which suggests that a high-quality flake is present. Nevertheless, a point defect, indicated with an arrow, can be found. It is represented by the increase of in topography (a) an the decrease of the signal voltage in (b).

The depression in topology is again about substrate holes. In the comparison of the two images in figure 38, it is striking that some holes are accompanied by a slight decrease in the near-field signal. The circled area emphasizes the depression of the near-field signal for a whole with a prominent depression. This phenomenon can also be found for other substrate holes, but it is less or hardly pronounced.

What does this observation mean? It is proof of the strong influence of the substrate on the dielectric function of atomic thin films. The dielectric function of the heterostructure WS_2 and SiO_2 has a distinct imaginary part for the energy in the range of the A exciton, as discussed in section 2.1. If the substrate-sample interaction has no alternating effect due to a sufficiently deep substrate hole, the dielectric function is not a composition of the shape $\epsilon_{\text{sample}} \circ \epsilon_{\text{substrate}}$ anymore, but $\epsilon_{\text{sample}} \circ \epsilon_{\text{vacuum}}$. This is shown as exemplary in figure 39.

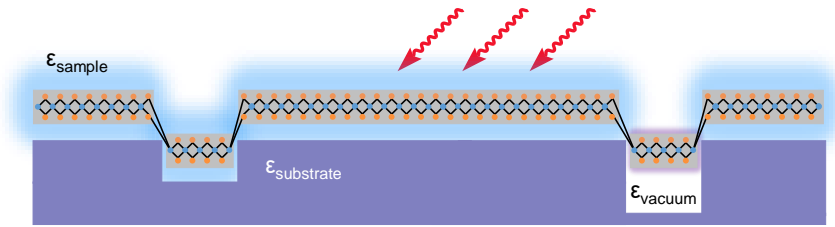


Figure 39: Illustration of the interactions of the dielectric function between the monolayers or multilayers of the sample with the substrate and the vacuum.

Conclusion

In this section it was shown that not only the sample but also the substrate quality plays an important role in the optical properties. If particularly deep substrate holes covered with WS_2 are present, the s-SNOM images, which otherwise show no optical signals, may become visible. This implies a change in the electronic sample characteristics and must be considered for further applications.

11 AFM imaging of ultra-thin terylene layers

In this chapter, an AFM study of terylene thin films deposited on glass is reported. The molecules have been evaporated for 20 min at 240 °C on a sapphire substrate using a KNUDSEN cell. [76]

11.1 Surface characterization

The crystalline structure of an organic semiconductor deposited on a dielectric substrate is strongly dependent on the dielectric surface properties. [77] The film growth and the orientation of the molecules determine the morphology of the layers.

As such, the topography of terylene was investigated by in situ AFM tapping mode measurements using a PtIr tip. Figure 40 shows (a) the surface topography and (b) the adhesion image with $2 \times 2 \mu\text{m}$ size that was scanned using 200×200 pixels. The transversal resolution is about 10 nm, which is limited by the tip radius.

The topography shows insular structures with a height up to approximately 11 nm. The aggregates are self-contained but irregularly shaped and can have a diameter of up to 600 nm. The mechanical phase shift reflects the shape of the insular grains. In figure 40c, the surface pattern of the surface morphology along a path with a length of $d = 2 \mu\text{m}$ is sketched.

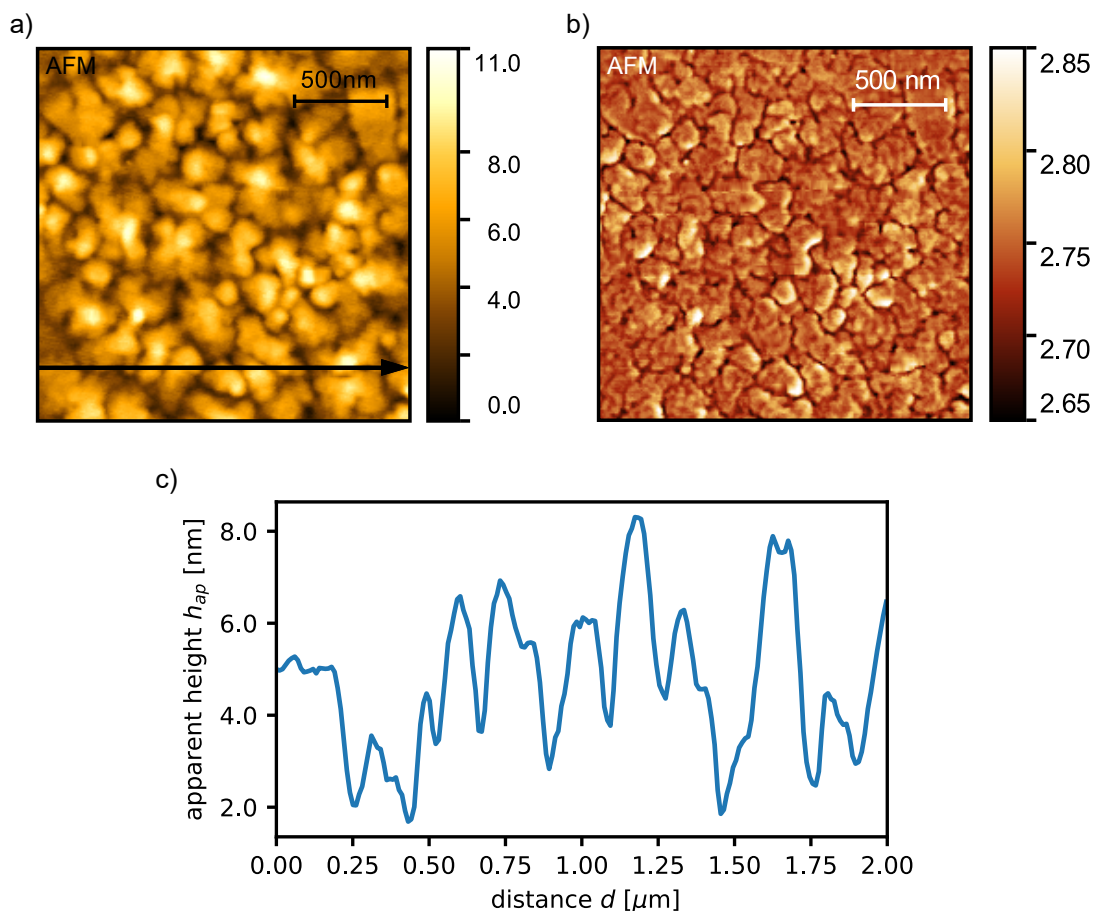


Figure 40: (a) Topography image of terylene. The color bar displays the apparent height in nm; (b) Mechanical phase image of terylene. The color bars displays angles in rad. (c) Cross-section of the topography along the path in (a).

The assembly of terylene is to this day unknown. The molecular packing of aromatic molecules depends on several factors. Many aromatic molecules are present in an edge-to-face configuration, the so-called herringbone configuration. This configuration results from intermolecular CH- π interactions, which are favored in highly stacked systems. This type of self-arrangement has already been observed for quaterylene molecules on a SiO₂ substrate [78] but, to best of the author's knowledge, not yet for a terylene sample or for a sapphire substrate. The authors performed AFM studies that interestingly resolved similar structures as shown in Figure 40a. This is an indication that terylene is also present in the herringbone configuration - which seems reasonable by the comparable CH- π interactions to the chemically related quaterylene. However, further studies need to be conducted to validate this hypothesis.

The root-mean-squared roughness (RMSR) is a characterization of the unevenness of the surface height. The larger the value, the larger the roughness. The RMSR S_q is defined as

$$S_q = \sqrt{\frac{1}{J \cdot K} \sum_{j=1}^J \sum_{k=1}^K \{h(x_j, y_k) - \langle h \rangle\}^2}, \quad (23)$$

where $h(x_j, y_k) = h_{jk}$ are the matrix entries at different sample coordinates and $\langle h \rangle$ is the mean value of the height for all matrix entries. Because of the formation of the aggregates, an RMSR value $S_q \approx 1.7$ nm is obtained for terrylene. Compared to other samples, such as quaterrylene desorbed at higher temperatures [78], the RMSR value is in the same order of magnitude. A three-dimensional image of the surface morphology illustrates the hilly structure, see figure 41.

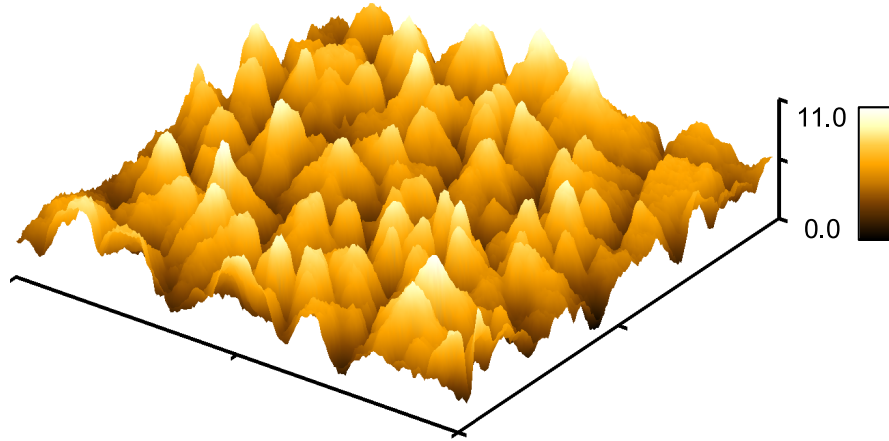


Figure 41: Three-dimensional representation of the topography (from figure 40a) of terrylene. The color bar displays the apparent height in nm.

11.2 Estimation of the layer thickness

A scratch was added to the sample to determine the mean thickness of the layer produced. The value determined by AFM was then compared with the results of established methods to determine whether the step height measurements are reliable.

A second-hand cantilever was placed in a holder and carefully stroked over the sample surface to inflict the scratch. The substrate-sample edge was examined by a PtIr tip using tapping mode AFM. The scan range of 200×200 pixels and a theoretical transversal resolution of 10 nm were maintained. The scratch is clearly visible in figure 42a. In addition, elevations in the topography can be observed. These are sample remnants that were thrown up during scribing. It should be noted that the color bar was adjusted for the topography image so that negative values are also included. The substrate surface should actually be assigned a height value of $h = 0$ nm. The reason lies in the sample remnants, which have a distinctive topography and would therefore deteriorate the contrast of the image.

In figure 42b, the cross-sectional profile of the topography is shown along a path of length $d = 1.5 \mu\text{m}$, see (a). In addition, a sigmoid fit function according to BOLTZMANN was laid through the profile.

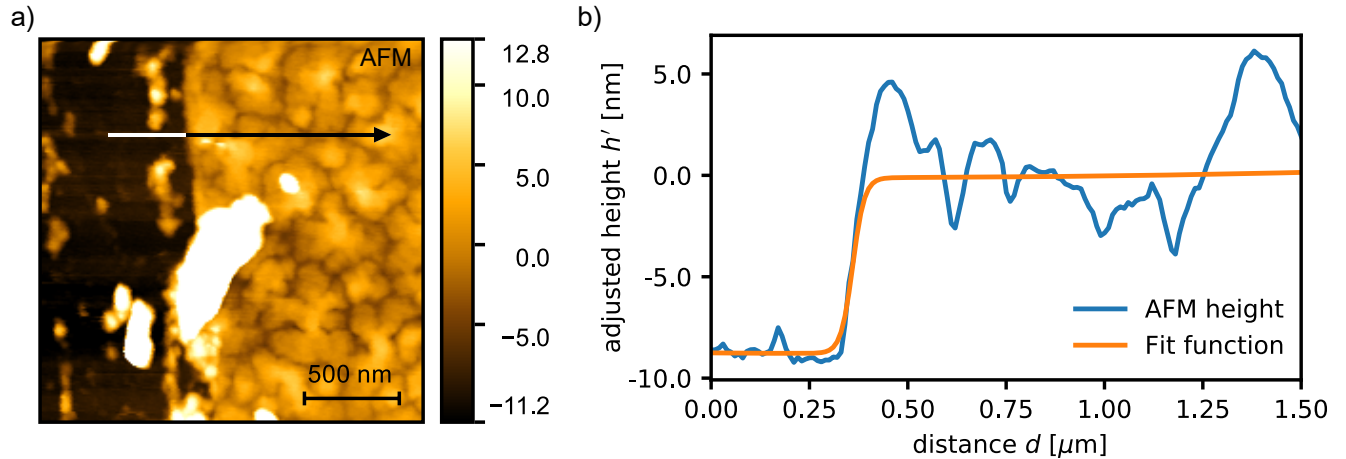


Figure 42: (a) Topography image of terrylene. The color bar displays the adjusted height h' in nm; (b) Cross-section of the topography (blue) and the corresponding fit function according to BOLTZMANN (orange).

The fit function suggests an average sample height of $\Delta h \simeq 8.7$ nm. The height was also determined through a quartz crystal microbalance by B. T. BONKANO. He found a mean substrate height of 8.64 nm.

Summary

In summary, the terrylene sample was scratched to determine the mean sample height. The comparison with quartz crystal microbalance measurements shows that AFM agrees with the results of other measurement methods. In this case, the apparent height of the topography corresponds to the actual sample height.

12 Summary and outlook

This work had two main components: the commissioning of a s-SNOM and its characterization with respect to different measurement methods, namely, self-homodyne and pseudo-heterodyne detection; the other, the comparison of high-resolution topography and lateral microscopy images of the analyzed systems. As the work is considered as a step towards studying the HIOS WS_2 /terrylene, a characterization of the individual samples was carried out.

A specific TMDC was examined after different reflection contrast spectra for the same flake were obtained. Using AFM, spatial heterogeneities on the microscopic length scale were resolved, explaining the finding of conventional microscopy: because of the large beam radius, dissimilar areas of the sample were considered for different measurements.

Scattering-SNOM measurements in a self-homodyne manner provided in situ topological and optical information for the first time in this thesis. An anticorrelation between topology and near-field magnitude was found, but with exceptions. However, at this point in time, no phase difference has been received. Through ex situ phase difference measurements and theoretical investigations of the HAMAKER constant,

the hypothesis that a change in the optical properties due to strong near-field enhancement of monolayers can also be detected with AFM was developed.

Because spatially dependent background scatter cannot be excluded in self-homodyne detection, self-homodyne and pseudo-heterodyne detection were compared. The extension of the experimental setup and using a HeNe laser instead of a diode laser reduced the problematic noise in pseudo-heterodyne to about the self-homodyne level. Then, it was demonstrated that the self-homodyne technique contains spatially dependent background scatter that is not present in pseudo-heterodyne detection.

Then, ultra-resolved topographic, mechanical and near-field amplitude mappings were recorded and compared. With the help of the improved results, it was concluded that the anticorrelation between topology and near-field amplitude is very likely. There are deviations because the apparent height of AFM topography images do not reflect the actual sample thickness as substrate fluctuations are also measured. These considerations are supported by measurements of the mechanical phase

The sample and substrate quality plays an important role in optical properties. Defects can alter the optoelectronic properties and were therefore characterized using AFM and s-SNOM. Here, deep substrate holes covered with WS₂, which are not present in the topography, were documented in near-field-amplitude mappings.

The results show that AFM or s-SNOM alone are not sufficient to distinguish between actual or apparent defect-induced sample properties. Both are needed to provide meaningful information about the sample properties.

Finally, the topography of thin film terylene was examined by AFM measurements. Based on those, it was proposed that terylene film deposited on sapphire are present in herringbone-configuration. Also, the terylene sample was scratched to determine the mean height. In this case, the apparent height of the topography is equal to the sample height.

In conclusion, this thesis provides an initial step towards the study of HIOS via s-SNOM. On the one hand, a deeper understanding of the properties of both an organic and an inorganic sample was obtained. The characterization of the sample and substrate quality provides important information about the influence of manufacturing and defects on the optoelectronic behavior. Moreover, the commissioning and characterization of the s-SNOM with respect to pseudo-heterodyne detection is the basis for the tracking of state transitions in HIOS. Because near-field mapping is heavily background polluted in the visible spectrum, pseudo-heterodyne detection will also be used for the investigation of HIOS as well, which is why its establishment represents an experimental advance.

By characterizing new samples, low defect WS₂ flakes will be identified. The next step is the deposition of terylene on WS₂. Using s-SNOM, the electron dynamix of the terylene/WS₂ HIOS will be studied with spatial resolution. In the medium term, time-resolved studies using pulsed laser sources will be carried out. This will be the world's first time-resolved s-SNOM in the visible range.

References

- [1] R. P. Feynman. *Engineering and Science* **1960**, 23(5), 22–36.
- [2] The Nobel Prize in Physics 2010: <https://www.nobelprize.org/prizes/physics/2010/summary/>. (15.11.2019).
- [3] J. Gu, B. Chakraborty, M. Khatoniar, V. M. Menon. *Nat. Nanotechnol.* **2019**, 14(11), 1024–1028.
- [4] D. Ochoa, R. Houdré, M. Ilegems, C. Hanke, B. Borchert. *C. R. Phys.* **2002**, 3(1), 3–14.
- [5] Collaborative Research Centre 951: <https://www.physik.hu-berlin.de/de/sfb951>. (15.11.2019).
- [6] G. Binnig, C. F. Quate, Ch. Gerber. *Phys. Rev. Lett.* **1986**, 56(9), 930–933.
- [7] Q. Zhong, D. Inniss, K. Kjoller, V. B. Elings. *Surf. Sci. Lett.* **1993**, 290(1-2), 688–692.
- [8] G. Haugstad. *Atomic force microscopy Exploring basic modes and advanced applications*; John Wiley & Sons: Hoboken, 2012.
- [9] F. London. *Z. Physik* **1930**, 63(3-4), 245–279.
- [10] P. Debye. *Phys. Ztschr.* **1920**, 21, 178–187.
- [11] W. H. Keesom. *Proc. R. Acad. Sci.* **1915**, 18, 636–646.
- [12] W. Pauli. *Z. Physik* **1925**, 31(1), 765–783.
- [13] J. E. Lennard-Jones. *Proc. Phys. Soc.* **1931**, 43(5), 461–482.
- [14] E. H. Synge. *Lond. Edinb. Dubl. Phil. Mag.* **1928**, 6(35), 356–362.
- [15] D. W. Pohl, W. Denk and M. Lanz. *Appl. Phys. Lett.* **1984**, 44(7), 651–653.
- [16] Y. Inouye, S. K. *Opt. Lett.* **1994**, 19(3), 159ff.
- [17] N. Behr, M. B. Raschke. *J. Phys. Chem. C* **2008**, 112(10), 3766–3773.
- [18] R. Hillenbrand, T. Taubner, F. Keilmann. *Nature* **2002**, 418(6894), 159–162.
- [19] E. Yoxall. *Dissertation: Applications of Scattering-Type Scanning Near-Field Optical Microscopy in the Infrared*; Imperial College London (Department of Physics), 2013.
- [20] L. Gomez, R. Bachelot, A. Bouhelier, G. P. Wiederrecht, S. Chang, S. Gray, F. Hua, S. Jeon, J. A. Rogers, M. E. Castro, S. Blaize, I. Stefanon, G. Lerondel, P. Royer. *J. Opt. Soc. Am. B* **2006**, 23(5), 823–833.
- [21] R. Hillenbrand, B. Knoll, F. Keilmann. *J. Microsc.* **2001**, 202(1), 77–83.
- [22] A. Cvitkovic, N. Ocelic, R. Hillenbrand. *Opt. Express* **2007**, 15(14), 8550–8565.
- [23] J. M. Stiegler. *Dissertation: Infrared spectroscopic near-field microscopy of nanoparticles and semiconductor nanowires*; University of the Basque Country (Materials Physics Department), 2012.
- [24] M. B. Raschke, C. Lienau. *Appl. Phys. Lett.* **2003**, 83(24), 5089–5091.

- [25] S. C. Lippert. *Dissertation: Optical Spectroscopy on chalcogens and porphyrins*; Philipps-Universität Marburg, 2018.
- [26] J. A. Wilson, A. D. Yoffe. *Adv. Phys.* **1969**, 18(73), 193–335.
- [27] N. A. Pike, A. Dewandre, B. van Troeye, X. Gonze, M. J. Verstraete. *Phys. Rev. Materials* **2019**, 3(7), 1601832.
- [28] B. Mahler, V. Hoepfner, K. Liao, O. Kristine, G. A. Ozin. *J. Am. Chem. Soc.* **2014**, 136(40), 14121–14127.
- [29] S. S. Chou, N. Sai, P. Lu, E. N. Coker, S. Liu, K. Artyushkova, T. S. Luk, B. Kaehr, C. J. Brinker. *Nat. Commun.* **2015**, 6(1), 8311.
- [30] G. Plechinger, J. Mann, E. Preciado, D. Barroso, A. Nguyen, J. Eroms, C. Schüller, L. Bartels, T. Korn. *Nanotechnology* **2014**, 29(6), 064008.
- [31] R. A. Bromley, R. B. Murray, A. D. Yoffe. *Adv. Phys.* **1972**, 5(7), 759–778.
- [32] H. Terrones, F. López-Urías, M. Terrones. *Sci. Rep.* **2013**, 3, 1549.
- [33] G. Wang, A. Chernikov, M. M. Glazov, T. F. Heinz, X. Marie, T. Amand, B. Urbaszek. *Nat. Commun.* **2018**, 9(2), 673.
- [34] Y. C. Cheng, Q. Y. Zhang, U. Schwingenschlögl. *Phys. Rev. B* **2014**, 89(15).
- [35] Z. Y. Zhu, Y. C. Cheng, U. Schwingenschlögl. *Phys. Rev. B* **2011**, 84(15), 78.
- [36] J. P. Echeverry, B. Urbaszek, T. Amand, X. Marie, I. C. Gerber. *Phys. Rev. B* **2016**, 93(12), 3878.
- [37] W. Tang. *Master Thesis: ELECTRICAL, ELECTRONIC and OPTICAL PROPERTIES OF MoS₂ & WS₂*; New Jersey Institute of Technology (Materials Science and Engineering), 2017.
- [38] A. Chernikov, T. C. Berkelbach, H. M. Hill, A. Rigosi, Y. Li, O. B. Aslan, D. R. Reichman, M. S. Hybertsen, T. F. Heinz. *Phys. Rev. Lett.* **2014**, 113(7), 076802.
- [39] W. Zhao, Z. Ghorannevis, L. Chu, M. Toh, C. Kloc, P.-H. Tan, G. Eda. *ACS nano* **2013**, 7(1), 791–797.
- [40] L. Kador, A. Müller, W. Richter. *Mol. Cryst. Liq. Cryst.* **1996**, 291(23).
- [41] S. Kummer, F. Kulzer, R. Kettner, Th. Basché, C. Tietz, C. Glowatz, C. Kryschi. *J. Chem. Phys.* **1997**, 107(19), 7673–7684.
- [42] McHale, J. L. *Molecular Spectroscopy, Second Edition*; CRC Press: Baton Rouge, 2nd ed. ed., 2017.
- [43] M. A. Kol'chenko, B. Kozankiewicz, A. Nicolet, M. Orrit. *Opt. Spectrosc.* **2005**, 98(5), 681.
- [44] L. Foglia. *Dissertation: Ultrafast dynamics and energy loss channels at a hybrid organic inorganic interface*; TU Berlin (Faculty of Mathematics and Natural Sciences), 2015.
- [45] F. M. Etzler, J. Drelich. *Developments in Surface Contamination and Cleaning; Chapter 6 - Atomic Force Microscopy for Characterization of Surfaces, Particles, and Their Interactions*; Elsevier, 2012.
- [46] R. García, A. San Paulo. *Phys. Rev. B* **1999**, 60(7), 4961–4967.

References

- [47] B. Voigtländer. *Scanning probe microscopy Atomic force microscopy and scanning tunneling microscopy*, NanoScience and technology; Springer: Heidelberg, 2015.
- [48] A. Varol, I. Gunev, B. Orun, C. Basdogan. *Nanotechnology* **2008**, 19(7), 075503.
- [49] R. García. *Surf. Sci. Rep.* **2002**, 47(6-8), 197–301.
- [50] B. Anczykowski, B. Gotsmann, H. Fuchs, J. P. Cleveland, V. B. Elings. *Appl. Surf. Sci.* **1999**, 140(3-4), 376–382.
- [51] G. K. H. Pang, K. Z. Baba-Kishi, A. Patel. *Ultramicroscopy* **2000**, 81(2), 35–40.
- [52] B. Knoll, F. K. *Opt. Commun.* **2000**, 182(4-6), 321–328.
- [53] M. Labardi, S. Patanè, M. Allegrini. *Appl. Phys. Lett.* **2000**, 77(5), 621–623.
- [54] R. Hillenbrand, F. *Phys. Rev. Lett.* **2000**, 85(14), 3029–3032.
- [55] B. Bhushan, H. Fuchs, M. Tomitori. *Applied scanning probe methods VIII; Scanning probe microscopy techniques*, Nanoscience and technology; Springer-Verlag: Berlin, Heidelberg, 2008.
- [56] G. Dai, Z. Yang, G. Geng, M. Li, T. Chang, D. Wei, C. Du, C. Chunlei, H.-L. Cui, H. Wang. *Appl. Spectrosc. Rev.* **2018**, 53(10), 806–835.
- [57] N. Ocelic, A. Huber, R. Hillenbrand. *Appl. Phys. Lett.* **2006**, 89(10), 101–124.
- [58] NeaSpec: <https://www.neaspec.com>. (**21.09.2019**).
- [59] Wedler, G. *Lehrbuch der physikalischen Chemie*; Wiley-VCH: Weinheim, 4th ed., 1997.
- [60] A. Einstein. *Phys. Ztschr.* **1917**, (121), 167–183.
- [61] Christian Gerthsen, D. M. *Physik Mit ... 94 Tabellen ... und Visualisierungen der Relativitätstheorie auf CD-ROM; [die ganze Physik zum 21. Jahrhundert*, Springer-Lehrbuch; Springer: Berlin, 23th ed., 2006.
- [62] Spectrum Instrument: <http://www.ntmdt-tips.com/products/view/tgq1>. (**17.09.2019**).
- [63] oral communication: S. Palato. (**28.08.2019**).
- [64] D. Sarid, W. A. Challener. *Modern introduction to surface plasmons Theory, Mathematica modeling and applications*; Cambridge University Press: Cambridge, 2010.
- [65] R. J. Hermann, J. G. Michael. *Opt. Express* **2018**, 26(21), 27668–27682.
- [66] NanoWorld: <https://www.nanoandmore.com/AFM-Probe-ARROW-NCpt>. (**21.10.2019**).
- [67] MikroMasch OPUS: <https://www.nanoandmore.com/AFM-Tip-160AC-GG>. (**21.10.2019**).
- [68] D. E. Tranca, S. G. Stanciu, R. Hristu, C. Stoichita, S. A. M. Tofail, G. A. Stanciu. *Sci. Rep.* **2015**, 5, 11876.
- [69] D. I. Yakubovsky, A. V. Arsenin, Y. V. Stebunov, D. Y. Fedyanin, V. S. Volkov, Valentyn S.. *Opt. Express* **2017**, 25(21), 25574–25587.

- [70] E. Pensa, E. Cortés, G. Corthey, P. Carro, C. Vericat, M. H. Fonticelli, G. Benítez, A. A. Rubert, R. C. Salvarezza. *Acc. Chem. Res.* **2012**, *45*(8), 1183–1192.
- [71] G. Kortüm, W. Braun, G. Herzog. *Angew. Chem.* **1963**, *75*(14), 653–661.
- [72] Y. Li, X. Li, T. Yu, G. Yang, H. Chen, C. Zhang, Q. Feng, J. Ma, W. Liu, H. Xu, Y. Liu, X. Liu. *Nanotechnology* **2018**, *29*(12), 124001.
- [73] Y.-C. Lin, C.-H. Yeh, H.-C. Lin, M.-D. Siao, Z. Liu, H. Nakajima, T. Okazaki, M.-Y. Chou, K. Suenaga, P.-W. Chiu. *ACS nano* **2018**, *12*(12), 12080–12088.
- [74] J. Yang, P. Gordiichuk, O. Zheliuk, J. Lu, A. Herrmann, J. Ye. *Phys. Status Solidi RRL* **2017**, *11*(10), 1700302.
- [75] I. Buyanova, J. Stehr, W. Chen., Ed. *Defects in Advanced Electronic Materials and Novel Low Dimensional Structures*; Woodhead Publishing (an imprint of Elsevier): Duxford, United Kingdom, 2018.
- [76] oral communication: B. T. Bonkano. (**14.11.2019**).
- [77] H. Yang, T. J. Shin, M.-M. Ling, K. Cho, Kilwon, C. *J. Am. Chem. Soc.* **2005**, *127*(33), 11542–11543.
- [78] R. Hayakawa, M. Petit, Y. Wakayama, T. Chikyow. *Org. Electron.* **2007**, *8*(5), 631–634.

List of figures

1	Schematic setup of an AFM.	3
2	6,12-LENNARD-JONES Potential.	4
3	Schematic setup of a s-SNOM.	5
4	Illustration of the dipole model.	6
5	(a) Hexagonal close-packed crystal structure with a highlighted unit cell; (b) Hexagonal 2H WS ₂ monolayer seen from the side.	7
6	Schematic band structure of 2H WS ₂ along (a) a one-dimensional path of high symmetry, after ref. [32], and (b) the base vectors k_x and k_y	8
7	Schematic representation of the splitted bands, with the approximation that $\Delta_{VB} = 0$ eV.	9
8	Imaginary part of the dielectric function $\text{Im}(\epsilon(E))$ of 2H WS ₂ on SiO ₂ , after ref. [37].	9
9	Schematic representation of an exition as well as $\epsilon_{\text{sample}}(f)$ for (a) monolayers and (b) multilayers.	10
10	Skeletal formula of terrylene.	11
11	(a) Illustration of the electron dynamix within vibronic levels in terrylene; (b,c) Absorption and PL spectrum of terrylene in solution. The measurement data were received from B. T. BONKANO.	11
12	(a) Influence of quality factor Q (with $Q_1 > Q_2$) on the cantilever amplitude A_{cant} and phase difference ϕ ; (b) Schematic representation of the amplitude modulation operation mode.	15
13	Simulated FOURIER transform of the (self-homodyne) signal intensity $I_d(t)$, revealing the harmonics $n\Omega$ in the frequency-domain. Here, the intensity $I_d(f)$ was converted into a signal voltage $U(f)$ by the detector.	16
14	Schematic detection scheme for pseudo-heterodyne detection. No more than a reference arm has been added to the setup.	18
15	Simulated FOURIER transform of the pseudo-heterodyne signal intensity $I_d(t)$, revealing the harmonics $n\Omega$ and the sidebands mM in the frequency-domain.	18
16	Schematic illustration of the optical setup. The abbreviations stand for: BS - beam splitter; PD – photodiode; ND – neutral density; RM – reference mirror; PM - parabolic mirror.	20
17	Illustration of the EINSTEIN coefficients using a three-level system.	20
18	Mechanical phase images of TGQ1 with (a) an intact tip and (b) a damaged tip. The color bar displays angles in rad.	23
19	Optical approach-curves (measured in self-homodyne manner) showing the detected signal voltage U ; the blue one contains little background scatter and the orange much.	24
20	Optical images at the fourth-harmonic demodulation of TGQ1 with (a) a high SNR and (b) a low SNR. The color bar displays voltages in mV.	24

21	Mechanical approach curves showing the cantilever amplitude. The blue graph A_{cant}^1 refers to a PtIr tip and the orange one A_{cant}^2 to a gold tip.	26
22	Optical image of a homogeneous WS ₂ triangle.	29
23	Reflection spectra of different measurement series for the same WS ₂ flake. The measurement data were received from S. CALATI.	30
24	Optical image of the WS ₂ flake with an optical microscope that can resolve the spatial inhomogeneities.	31
25	Cross-section of the topography (blue) and the corresponding fit function according to BOLTZMANN (orange).	31
26	Cross-section of the topography (blue) and the corresponding fit function according to BOLTZMANN (orange).	32
27	Schematic illustration of the cause for the shift of the A exciton in the reflection spectra. . .	32
28	(a) Optical image of the WS ₂ flake; (b) Topography image of WS ₂ /SiO ₂ . The color bar displays the apparent height in nm; (c) Optical image of WS ₂ /SiO ₂ at the third-harmonic demodulation. The color bar displays voltages in mV; (d) Mechanical phase image of WS ₂ /SiO ₂ . The color bar displays angles in rad.	34
29	(a, b) Cross-sections of the topography (blue) and near-field magnitude (orange) along the paths 1 and 2, respectively.	35
30	Mechanical phase images of WS ₂ /SiO ₂ . The color bar displays angles in rad.	35
31	Optical images of WS ₂ /SiO ₂ using (a) self-homodyne detection at the third-harmonic demodulation and (b) pseudo-heterodyne detection at the fourth-harmonic demodulation. The color bar displays voltages in mV.	38
32	Optical approach curves showing the detected signal voltage U for self-homodyne (blue) and pseudo-heterodyne (orange) detection.	38
33	NMD of the near-field magnitude (blue) and near-field amplitude (orange) along a homogeneous 2 nm path on SiO ₂	39
34	(a) Optical image of WS ₂ /SiO ₂ at the fourth-harmonic demodulation. The color bar displays voltages in mV; (b) Optical image of WS ₂ at the fourth-harmonic demodulation. The color bar displays voltages in mV; (c) Topography image of WS ₂ . The color bar displays the apparent height in nm; (d) Mechanical phase image of WS ₂ . The color bar displays angles in rad.	40
35	Illustration of the findings in this chapter.	41
36	Schematic illustration of equilibrium defect concentration c_d^{eq} according to the GIBBS-HELMHOLTZ equation.	42
37	(a, b) Mechanical phase images of defects in WS ₂ ; (c) Mechanical phase image of a low-defect WS ₂ flake, including SiO ₂ . All color bars display angles in rad.	43

List of figures

38	(a) Topography image of WS ₂ /SiO ₂ . The color bar displays the apparent height in nm; (b) Optical image of WS ₂ /SiO ₂ at the fourth-harmonic demodulation. The color bar displays voltages in mV.	44
39	Illustration of the interactions of the dielectric function between the monolayers or multilayers of the sample with the substrate and the vacuum.	45
40	(a) Topography image of terrylene. The color bar displays the apparent height in nm; (b) Mechanical phase image of terrylene. The color bars displays angles in rad. (c) Cross-section of the topography along the path in (a).	46
41	Three-dimensional representation of the topography (from figure 40a) of terrylene. The color bar displays the apparent height in nm.	47
42	(a) Topography image of terrylene. The color bar displays the adjusted height h' in nm; (b) Cross-section of the topography (blue) and the corresponding fit function according to BOLTZMANN (orange).	48

Acknowledgments

A lot of people joined me on this bachelor thesis writing journey and gave me nothing but their whole support and this cannot be forgotten. That is why I would like to express my immense gratitude for the help and assistance.

First of all, I want to thank JULIA so much for allowing me to be a part of her working group, for all her helpful suggestions, including the correction of my thesis, and especially for all the motivation when it was not going as it was supposed to.

I am very grateful that Prof. ECKART RÜHL and Dr. ROMAN FLESCHE agreed to supervise my thesis. Moreover, I would like to thank Prof. ECKART RÜHL for helping me with the organization of the thesis.

I highly appreciate everyone of JULIAS research group for so many things, such as the warm welcome, the great atmosphere and the tremendous helpfulness. I want to thank ANGELIKA, BOUBACAR, INES, JOACHIM, JULIA, LUKAS, SAM, STEFANO and RADOSLAW. A special thanks goes to SAM who has been there for me this whole time during the project and who never stopped to answer my (unending) questions: He showed me the methods of scientific working, showed me how to align optical constructions, showed me how to do data analysis with Python and Gwyddion and got me into science policy (and maybe fashion related stuff).

I have learned an incredible amount in this group in this short time and will remember this experience as one of the most valuable things of my undergraduate degree.

I also got a lot of aid from people outside of the working group. I want to thank DUYUM for proofreading and for giving me clues regarding the english language (which I hope was not too bad towards the end of the thesis). And I want to thank STEFAN for showing me how to make high-quality illustrations with ChemDraw. By the way: suddenly ☺.

Last but not least, I want to thank my mother from the bottom of my heart because she helped and supported me unconditionally since the very beginning and also gave me the opportunity to study.

Statutory declaration

I hereby declare that I have written the present thesis independently, without enlisting any external assistance, and only using the specified aids.

Place, Date

signature